MARMARA UNIVERSITY
INSTUTE FOR GRADUATE STUDIES

DESIGN AND CHARACTERIZATION OF ACTIVE PHOTOCATAYLYSTS BASED ON TRANSITION METAL CHALCOGENIDES

İREM TANIŞIK

MASTER THESIS

Department of Chemical Engineering

Thesis Supervisor

Prof.Dr.Atıf Koca

ISTANBUL, 2019

MARMARA UNIVERSITY
INSTUTE FOR GRADUATE STUDIES

DESIGN AND CHARACTERIZATION OF ACTIVE PHOTOCATAYLYSTS BASED ON TRANSITION METAL CHALCOGENIDES

İREM TANIŞIK

(524516016)

MASTER THESIS

Department of Chemical Engineering

Thesis Supervisor

Prof.Dr.Atıf Koca

ISTANBUL, 2019

MARMARA UNIVERSITY

INSTITUTE FOR GRADUATE STUDIES IN PURE AND APPLIED SCIENCES

İrem TANIŞIK, a Master of Science student of Marmara University Institute for Graduate Studies in Pure and Applied Sciences, defended her thesis entitled "**Design and Characterization of Active Photocatalysts Based on Transition Metal Chalcogenides**", on June 17, 2019 and has been found to be satisfactory by the jury members.

Jury Members

Prof. Dr. Atıf KOCA (Advisor)
Marmara University .....(SIGN) .....

Prof. Dr. Hüseyin DELİGÖZ (Jury Member)
Istanbul University .....(SIGN) .....

Prof. Dr. Fatma KARACA ALBAYRAK (Jury Member)
Marmara University .....(SIGN) .....

APPROVAL

Marmara University Institute for Graduate Studies in Pure and Applied Sciences Executive Committee approves that İrem TANIŞIK be granted the degree of Master of Science in Department of Chemical Engineering, Chemical Engineering Program on July 0, 2019. (Resolution no: 2019/14-02).

Director of the
Institute Prof. Dr. Adı

Prof. Dr. Bülent EKİCİ
Enstitü Müdürü

MARMARA ÜNİVERSİTESİ
FEN BİLİMLERİ ENSTİTÜSÜ

Marmara Üniversitesi Fen Bilimleri Enstitüsü Yüksek Lisans Öğrencisi İrem TANIŞIK'ın "**Fotokatalitik Hidrojen Üretimi İçin Sülfürizasyon Yöntemi ile Fotokatalizörlerin Üretilmesi ve Karakterizasyonu**" başlıklı tez çalışması, 17 Haziran 2019 tarihinde savunulmuş ve jüri üyeleri tarafından başarılı bulunmuştur.

Jüri Üyeleri

Prof. Dr. Atıf KOCA (Danışman)
Marmara Üniversitesi .....(İMZA).....

Prof. Dr. Hüseyin DELİGÖZ (Üye)
İstanbul Üniversitesi .....(İMZA).....

Prof. Dr. Fatma KARACA ALBAYRAK (Üye)
Marmara Üniversitesi .....(İMZA).....

ONAY

Marmara Üniversitesi Fen Bilimleri Enstitüsü Yönetim Kurulu'nun 10/07/2019 tarih ve 2019/14-02 sayılı kararı ile İrem TANIŞIK'ın Kimya Mühendisliği Anabilim Dalı, Kimya Mühendisliği Programında Yüksek Lisans derecesi alması onanmıştır.

Fen Bilimleri Enstitüsü Müdürü Prof. Dr. Adı SOYADI

Prof. Dr. Bülent EKİCİ
Enstitü Müdürü

ACKNOWLEDGMENT

First of all, I would like to express my sincere gratitude to my supervisor, Prof. Dr. Atıf Koca for all his guidance, support and motivation throughout my research.

I would like to thank to TUBİTAK for their supports in project called "Fotoelektrokimyasal-Fotokatalitik Hidrojen Üretim Reaksiyonları (PEPCHER) ile Saf HidrojenÜretimi" (Project Number: 116M567). I sincerely thank Prof. Dr. Cevat Sarığlu, Prof. Dr. Fatma Karaca Albayrak, Prof. Dr. Ali Rıza Özkaya for their encouragement in carrying out this project work. I am grateful to my friends Rana Muhammad Zunain Ayaz and Özlem Uğuz whom we collaborated together in this project. I would like to express my deepest appreciation to Duygu Akyüz who helped me to complete this report.

I also would like to thank to BAPKO for their supports in project called "Geçiş metali kalgojenlerinden oluşan aktif fotokatalizörlerin tasarlanması ve karakterizasyonu" (Project Number: FEN-C-YLP-090518-0248).

Lastly, I would like to thank my dear family; Şebnem Tanışık and Kudret Tanışık, who has not refrain their support to me in my education and whole life, trusting me in every subject and always proud of me and being proud to be a part of it.

May, 2019 **İrem TANIŞIK**

TABLE OF CONTENTS

ABSTRACT

DESIGN AND CHARACTERIZATION OF ACTIVE PHOTOCATALYSTS BASED ON TRANSITION METAL CHALCOGENIDES

The use of fossil fuels causes CO_2 emissions. In recent years, the tendency to use alternative energy sources has increased due to increased environmental concerns. Among the alternative energy sources, studies on hydrogen energy have accelerated. Hydrogen as an energy source is obtained both from fossil fuels or electrolysis of water. Up to today, hydrogen production has mostly been derived from fossil sources. However, since these approaches are considered as non-environmentally friendly, and clean; hydrogen energy in the energy sector has not been able to pay attention. In recent years, researches are concentrated on hydrogen production from water studies on the production of hydrogen from water by using solar energy have intensified.

In the photocatalytic hydrogen production, the catalysts have an important place. $Cd_xZn_{(1-x)}S$ is one of the most preferred photocatalysts due to their controllable band cavities and their excellent resistance to corrosion. Therefore, $Cd_xZn_{(1-x)}S$ and RGO-$Cd_xZn_{(1-x)}S$ photocatalysts were synthesized using different x values in this thesis study and hydrogen activities were analysed.

$Cd_xZn_{(1-x)}S$ photocatalysts with different compositions were synthesized by the thermal sulphurization technique and the these photocatalysts were decorated with reduced graphene oxide (RGO) to enhance photocatalytic activity. To determine crystal systems, lattice parameters, band spacing and surface morphologies, produced photocatalysts were characterized by X-Ray diffractometer (XRD), Ultraviole-visible (UV-VIS) spectrophotometer, scanning electron microscope (SEM) and Raman spectrophotometer. Subsequently, hydrogen efficiency of $Cd_xZn_{(1-x)}S$ and RGO-$Cd_xZn_{(1-x)}S$ composites were analysed.

Structures of photocatalysts were characterized by XRD, EDS and Raman spectra. Presence of RGO in RGO-$Cd_xZn_{(1-x)}S$ has proven by these analysis. As RGO has a high electron conductivity which increases electron transfer rate, adsorption capacity and extended light absorption range, RGO-$Cd_xZn_{(1-x)}S$ photocatalysts have higher photocatalytic activity. The RGO-$Cd_{0.7}Zn_{0.3}S$ photocatalyst having 2.86 eV band gap was found to be the most suitable photocatalyst for hydrogen production with 141.6

$\mu molh^{-1}$ hydrogen production and 19.4 % quantum efficiency. Since high crystallinity has observed from thermal sulphurization method, $Cd_{0.7}Zn_{0.3}S$ photocatalyst produced by thermal sulphurization method has higher rate of hydrogen production than $Cd_{0.7}Zn_{0.3}S$ photocatalysts produced by different methods.

ÖZET

GEÇİŞ METALİ KALGOJENLERİNDEN OLUŞAN AKTİF FOTOKATALİZÖRLERİN TASARIMI VE KARAKTERİZASYONU

Fosil yakıtların kullanımı CO_2 salınımına neden olmaktadır. Sonn yıllarda, artan çevre hassasiyetleri nedeniyle alternative enerji kaynaklarının kullanımına olan eğilim artmıştır.Alternatif enerji kaynakları arasında hidrojen enerjisine yönelik çalışmalar hız kazanmıştır. Enerji olarak hidrojen, fosil yakıtlardan veya suyun elektrolizinden elektrik enerjisi kullanılarak eldee dilmektedir. Bugüne kadar hidrojen üretimi çoğunlukla fosil kaynaklardan elde edilmiştir. Ancak bu yöntemler çevre dostu olarak değerlendirilmediği, sürdürülebilir ve temiz olmadığı için enerji sektöründe hidrojen enerjisi gereken ilgiyi görememiştir. Bu nedenle, son yıllarda güneş enerjisi ile sudan hidrojen üretimi için yapılan çalışmalar hız kazanmıştır.

Fotokatalitik hidrojen üretiminde katalizörler öenmli bir yere sahiptir. $Cd_xZn_{(1-x)}S$ control edilebilir bant boşlukları ve korozyona karşı mükemmeld ayanıklılıkları nedeniyle en çok tercih edile nfotokatalizörlerden biridir. Bu nedenle, bu tez çalışmasında farklı x değerleri kullanılarak $Cd_xZn_{(1-x)}S$ ve RGO- $Cd_xZn_{(1-x)}S$ fotokatalizörleri sentezlendi ve hidrojenaktiviteleri test edildi.

Farklı $Cd_xZn_{(1-x)}S$ fotokataliz bileşimleri, termal sülfürizasyon yöntemi ile sentezlenmiş olup $Cd_xZn_{(1-x)}S$ fotokatalizörleri fotokatalitik aktiviteyi arttırmak için indirgenmiş grafenoksit (RGO) üzerine dekore edilmiştir. Fotokatalizörlerin karakterizasyonu; yüzey morfolojileri, bant aralıkları ve kafes parametreleri hakkında bilgi sahibi olmak için X-Ray difraktometre (XRD), taramalı electron mikroskobu (SEM), ultraviyole-görünür (UV-VIS) spektrofotometre ve Raman spektrofotometre cihazları kullanılarak gerçekleştirilmiştir. Daha sonra, $Cd_xZn_{(1-x)}S$ ve RGO-$Cd_xZn_{(1-x)}S$ fotokatalizörlerinin hidrojen aktivitesine bakılmıştır.

XRD, EDS ve Raman spektrası yardımı ile fotokatalizörlerin yapıları belirlendi. RGO-$Cd_xZn_{(1-x)}S$ fotokatalizörlerinde RGO'nun varlığı kanıtlanmıştır. RGO, elektron transfer hızını, adsorpsiyon kapasitesini ve genişletilmiş ışık emme aralığını arttıran, yüksek bir electron iletkenliğine sahip olduğu için RGO-$Cd_xZn_{(1-x)}S$ fotokatalizörlerinin fotokatalitik aktivitesi daha yüksek bulunmuştur. 2.86 eV banta ralığına sahip olan RGO-

$Cd_{0.7}Zn_{0.3}S$ fotokatalizörü, 141.6 $\mu molh^{-1}$ hidrojen üretimi ve %19.4 kuantum verimi ile hidrojen üretimi için en uygun fotokatalizör olarak tespit edilmiştir. Termal sülfürizasyon metodu ile üretilen $Cd_{0.7}Zn_{0.3}S$ fotokatalizörünün kristalliği yüksek olduğu için farklı yöntemlerle üretilen $Cd_{0.7}Zn_{0.3}S$ fotokatalizörlerinden daha fazla hidrojen üretim hızına sahip olduğu gözlemlenmiştir.

SYMBOLS

ΔG	**:** Gibbs free energy
h^+	**:** hole
e^-	**:** electron
λ	**:** wavelength
E_g	**:** band gap of semiconductor
F(R)	**:** Kubelka-Munk function
h	**:** Planck's constant
v	**:** frequency of light
A	**:** constant value
R	**:** absolute reflectance
n	**:** integer number
d	**:** inter planar spacing
θ	**:** diffraction angle
n_F	**:** faradic efficiency
j_{sc}	**:** photocurrent density
α	**:** absorption coefficient
P	**:** power density
N_{eff}	**:** number of effective generated electron-hole pairs
N_{total}	**:** total number of incident photons
D	**:** average particle size
K	**:** crystallite shape factor
β	**:** full width at half maximum

ABBREVIATIONS

ABPE **:** Applied Bias Photon to Current Efficiency

AQE **:** Apparent quantum efficiency

CB **:** Conduction band

CRT **:** Cathode ray tube

EDS **:** Energy dispersive X-ray spectroscopy

FEG **:** Field emission gun

FWHM **:** Full width at half maximum

NHE **:** Normal hydrogen electrode

UV **:** Ultraviolet

SEM **:** Scanning electron microscopy

STH **:** Solar to hydrogen

PC **:** Photocatalytic

PEC **:** Photo electrochemical cell

QE **:** Quantum efficiency

XRD :X-ray diffraction

VB **:** Valance band

VIS **:** Visible

LIST OF FIGURES

LIST OF TABLES

1 INTRODUCTION

Energy sources can be categorized as primary and secondary energy sources. When the energy sources can be used directly, they are called primary energy sources which are divided into renewable and non-renewable energy sources. Renewable energy is the energy sources obtained from the existing energy flow in the natural processes and the energy resources that can be replenished once it is finished. On the other hand, non-renewable energy sources are energy sources that do not expire when consumed. Secondary energy sources that are derived from the transformation of primary energy sources like electric energy and hydrogen energy [1-5].

1.1 Hydrogen Energy

Hydrogen is the lightest and simplest element. It is found plenty in the nature. Compared to other alternative energy sources, hydrogen is clean and renewable since its major reserve, water, is inexhaustible. Due to the advantages listed below, it attracts a lot of attention among secondary energy sources:

- has high energy conversion efficiency,
- is accessible and clean energy,
- is easily converted to other energy forms,
- is renewable and sustainable energy sources,
- is less pollutant by not producing hydrocarbon
- is easily transported,
- is stocked both in liquid, gaseous or together with metal hydrides,
- is produced from water with no emissions,

Considering the growth in population along last decades, energy demand has been increased. However, fossil fuel reservoirs are limited and using fossil fuels leads to greenhouse gas emission causing a global warming. Nowadays, due to the environmental concerns, researches are devoted to find a sustainable supply of clean energy. To overcome environmental problems, there is an increasing interest on using renewable energy which is environment friendly [6-9]. Since the sun is primary and renewable energy source, photocatalytic hydrogen production has received more attention. Hydrogen is a secondary energy source which is obtained from different primary energy sources. Thereby, hydrogen considered as a secondary

energy source and act as an energy barrier. This barrier enables the energy to be transported, stored and delivered easily [9].

1.2 Hydrogen Production Methods

Hydrogen is produced using various processes. It can be obtained both renewable sources, nuclear energy or fossil fuels. Natural gas and coal are widely used for hydrogen production from fossil fuels. There are several ways such as to gasification of biomass, renewable electrolysis with electricity (wind, solar photovoltaic, solar thermal, geothermal, hydroelectric, and ocean systems), photochemical, photo electrochemical, thermochemical from solar and nuclear sources, biological and thermal decomposition methods obtain hydrogen from renewable sources. Each of these production techniques is the chemical conversion process of exhaustive sources [6, 10, 11].

In recent years, hydrogen energy is obtained principally by steam reforming gasification method. Steam reforming of natural gas comes from fossil fuels. For hydrogen energy production from fossil fuels, the following operations are performed: energy input, steam reforming and separation process. These processes yield carbon whose emission is one of the main causes of climate change, as a by-product. Firstly, carbon monoxide and carbo dioxide are formed by combining hydrogen with water vapor and oxygen. Then, hydrogen is separated from other substances [12].

In the case of hydrogen by nuclear sources, it is possible to obtain hydrogen by electrolysis via radioactive waste. With the developing technology, hydrogen production techniques through renewable energy sources are diversified. Thus, production portion with these methods increases [9].

Almost all of the remaining electrolysis and other methods are hydrogen derivative of renewable energy sources. To generate hydrogen from renewable sources, the electric energy is obtained by using water in the electrolysis of water or by breaking the water at high temperature or by burning the biomass to obtain hydrogen [13, 14].

Thermochemical process is the hydrogen production process by decomposition of water at temperatures exceeding 3000 K. The biggest problem with this process is that the materials required to perform the reaction cannot withstand the high temperature conditions. Another problem is that this process needs too much energy [8, 15].

The hydrogen from the biomass can be obtained by a gasification function. Biomass is processed in a reactor under high temperature and low pressure. After this process, hydrogen,

methane, CO_2, CO and N_2 gases are obtained. The heat obtains from the thermal and chemical reactions are directly used to generate hydrogen from organic materials. The very widespread example of this process is obtaining hydrogen from fossil fuels and biomass. Due to the high temperature of the gas streams, the hydrogen content is increased and very high purity hydrogen can be obtained after this process [16-18].

1.3 Hydrogen Production by Solar

Water splitting has become remarkable method in recent years. Water splitting can be examined in 3 ways: photobiological, thermochemical, and photochemical. In photobiological water splitting, plant and algae photosynthesis are used as the same process. It divided into two groups. These groups can be categorized as light dependent and light independent process. Direct and indirect biophotolysis compose the first processing, whereas dark fermentation is referred as second processing [19, 20].In general, photobiological systems use photosynthetic activity of bacteria and green algae for production of hydrogen. Photosynthetic systems are normally degrades CO_2 to carbon hydrates. The most effective photobiological systems for the production of hydrogen depends on green algae and microalgae such as cyano bacteria [21].

Another way of water splitting method is the light collecting system called photo electrochemical cell (PEC). This system provides a production of power required to electrolyse water. In similar structures, the anode or cathode of the light absorber semiconductor or both electrochemical can be located inside the cell. When the semiconductor photo electrode (anode or cathode) placed in the homogeneous electrolyte is illuminated by solar energy, PEC begins to produce enough voltage to decompose it into water molecules. Meanwhile, the other electrode is usually metal [22, 23].

Photocatalytic water splitting is another way to produce clean hydrogen from water. With this process, coherent efficiency of solar-to-hydrogen (STH) can be achieved with low cost. Moreover, this process provides a separate formation of hydrogen and oxygen during the reaction. It has a large market potential as it is suitable for small house systems with small reactor systems [20].

Due to these advantages, photocatalytic water splitting is more preferred than other water splitting methods such as photobiological and photo electrochemical. The details of the photocatalytic water splitting process will be explained in the next section.

1.4 Photocatalytic Water Splitting

We can delineate photocatalysis as a chemical reaction which is brought about by a photo irradiation when accompanied by a photocatalyst. The main functioning principle of photocatalysis is quite simple and can also be observed in nature on the plants that photosynthesize. Firstly, photons are absorbed for formation of electron hole pairs. Since most heterogeneous photocatalysts include properties which are semi-conductor, photocatalytic reactions progress on these materials. These semiconductors have a band structure. Via a band gap having favourable width, the conduction band (CB) is departed from the valence band (VB). If the energy of incident light is more significant than a gap hole has and electrons are produced in the CB which results in the formation of a (h^+) pair and an electron (e^-) hole, these electrons and holes which are photo generated induce redox reactions which are similar to electrolysis. In order to form H_2, water molecules are reduced by the electrons. For formation of O_2, water molecules are oxidized by holes so that overall water splitting is enabled. The original structure of photocatalyst abides, provided that the number of e- and h+ are coequally consumed. For this reason valance bands, conduction level and the band gap's width are the main important factors when it comes to semiconductor photocatalyst materials [15, 24, 25].

While the valence band's top level must be more positive than the redox potential of O_2/H_2O which is 1.23 V, conduction band's bottom level must be more negative than the redox potential of $H+/H_2$ (0 V vs. NHE). For this very reason water splitting requires minimum band gap of 1.23 eV, corresponding to light of circa 1100 nm [26].

$$\text{Band gap (eV)} = 1240/\lambda \text{ (nm)} \quad (1)$$

In order to delineate the efficiency for solar energy conversion, several terms have been adopted such as Applied Bias Photon-to-Current Efficiency (ABPE), and Quantum Efficiency (QE). Generally, ABPE is put to use for the characterization of a photo electrode material's photo-response yield under the influence of an applied voltage. ABPE is also termed as the photo-conversation efficiency occasionally. However, terms as such cannot be utilized to demonstrate the true photo-conversion yield when it comes to photocatalytic water splitting due to the voltage applied. Below equation describes the photo-conversion:

$$\eta_{ABPE}(\%) = \frac{(\text{Total power output} - \text{electrical power input})}{\text{light power input}} \text{ x } 100 \quad (2)$$

For quantum efficiency the photoactive films' characteristic photon conversion can be represented. It can be delineated as the incident photons' percentage and generated electrons when the photoactive films are being irradiated under a certain wavelength. This can be seen in equation below.

$$\eta_{ABPE}(\%) = \frac{N_{eff}}{N_{total}} \times 100 \quad (3)$$

Where N_{eff} represents effective generated electron-hole pair number under light irradiation whereas N_{total} represents total incident photons number.

From the equation above it can be observed that η_{QE} over passes the energy dissipation of solar irradiance as well as the chemical conversion efficiency. For this very reason it is favourable to qualify the photoactive films. However the efficiency of the water-splitting conversion should not be represented [20].

STH which referred as "solar-to-hydrogen" conversion yield is a term used to delineate the true hydrogen evolution efficiency of a water splitting reaction under the influence of sunlight. The description of STH can be seen under the equation 4.

$$STH = \left[\frac{\left|j_{sc}\left(\frac{mA}{cm^2}\right)\right| \times (1.23\ V) \times \eta_f}{P_{total}\left(\frac{mW}{cm^2}\right)}\right]_{AM1.5G} \quad (4)$$

where, power density of incident simulative sunlight at AM1.5G is represented by $P_{total,}$ photocurrent density production by j_{sc} and faradic efficiency as $\eta_{F.}$ For water splitting, thermodynamic voltage must be 1.23 V.

.Another form of STH conversion efficiency can also define with Equation 5:

$$STH = \left[\frac{(mmole\ H_2/s \times (237\ kJ/mole)}{P_{total}\left(\frac{mW}{cm^2}\right) \times Area\ (cm^2)}\right]_{AM1.5G} \quad (5)$$

As mentioned before, photocatalyst takes an active role in a photocatalytic water splitting reaction. Being non-corrosive, stable, abundant, environment friendly and cost-effective titania (TiO_2) has been frequently used as a photocatalyst. But first and foremost, energy levels of titania (TiO_2) are congruent to trigger the water-splitting reaction [21], meaning that the reduction energy level of water (EH^+/H_2 = 0 V) is not as positive as that of the CB of TiO_2

when the oxidation energy level of water (EO_2/H_2O = +1.23 V) is not as negative as that the VB. [20, 27, 28].

Despite the fact that TiO_2 has many disadvantages, the reason of its low efficiency of water-splitting when put under solar energy can be explained with the reasons stated below:

The first reason of the low water splitting efficiency is the fact that the electrons which are photo-generated existing in CB of TiO_2 have the possibility to recombine with the VB holes for releasing energy very fast in the form of unproductive photons or heat; Second, water's decomposition into hydrogen and oxygen is a chemical reaction which generates large positive Gibbs free energy as ΔG = 237 kJ/mole, hereby the backward reaction which is hydrogen and oxygen's recombination into water proceeds simply; the final, having TiO_2 a band gap of 3.2 eV allows the photocatalysts to be activated only under UV light. The UV light comprises almost 4% of solar spectrum. However, the contribution of visible light region to the solar spectrum is more or less 50%. The ability of TiO_2 to utilize on the UV region of solar spectrum compromises its potential to be an efficient photocatalyst as it only makes use of 4% of solar spectrum (Figure 1.1).

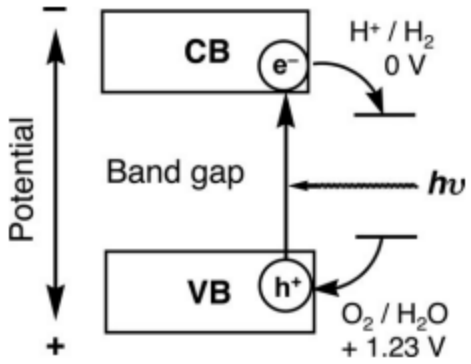

Figure 1.1. Mechnism of photocatalytic water splitting [29]

Band levels in oxide materials usually change when pH changes. TiO2, KTaO3, ZrO_2 and $SrTiO_3$ are modified by co-catalysts to make appropriate band structures for water separation. CdS may not be able to separate water into H_2 and O_2, although it behaves as if it has a suitable band position with a suitable band gap thanks to the visible light response. S_2 atoms in CdS oxidize H_2Oaccordingto the Equation 6 by elution of Cd^{2+}[29-31].

$$CdS + 2h^+ \rightarrow Cd^{2+} + S \qquad (6)$$

The reaction mentioned above is named photo corrosion which is usually a dilemma of metal sulfides. Furthermore, ZnO is an oxide, however the band gap excitation causes its photocorrosion.

$$ZnO + 2h^{+} \rightarrow Zn^{2+} + 1/2O_2 \quad (7)$$

On the other hand providing that a hole scavenger exists, CdS is an efficient photocatalyst when it comes to hydrogen generation under visible light irradiation.

Due to the low level of conductive band, WO_3 is an efficient photocatalyst for the evolution of O_2 under visible light irritation when there is an electron acceptor such as Fe^{3+} and Ag^{+} although it is inactive for the photocatalytic water splitting. In the case of the design of the photocatalyst, proper band engineering is a necessity since the photocatalyst working with a visible light should have a narrow gap of less than 3.0 eV [29].

In the second stage, photo generated carriers migrate and charges are separated to each other. The size of particle, crystallinity and crystal structure significantly affect this place. As quality of crystalline increases, the amount of defect decreases. The defects act as recombination centre to the photo generated charge carriers which in turn decrease the photocatalytic activity. Since probability of recombination depends on the distance between holes and photo generated electrons, decrease in particle size cause a decline in probability of recombination [32].

The last stage comprises of surface chemical reactions, which includes active sites (surface character) and surface area (the quantity) are very crucial for this process. Considering the situation have no or negligible active sites on the surface of photocatalyst, photo generated (electrons as a majority and holes as a minority) charge carriers, even though having enough potential for water splitting, will have to recombine. Since, several oxide-based photocatalysts do not possess the conduction band level as high as to reduce water to H_2. Therefore, in these cases, the use of catalyst (doping and/or loading) is an absolute necessity for solar light driven H_2 evolution reactions. For the motivation of creation active sites there are some famous and mostly used co-catalysts are present such as NiO, RuO_2 and Pt which are generally loaded or doped introduce active sites. Being an uphill reaction, the reaction between O_2 and evolved H_2 during the photocatalytic activity causes the back reactions which produces water resultantly. Considering this approach in mind, it can be said frail or poor properties of photocatalysts and co-catalysts surface cause reverse reaction [24, 28].

By the Figure 1.2, it can be observed how photocatalysts conditions in the case of TiO_2 affect the process. There are several methods that can be used to prepare the TiO_2 photocatalyst. Considering the example here that with process of hydrolysis, titanium tetra-isopropoxide amorphous TiO_2, which can be represented as $TiO_2.nH_2O$, is obtained. Some factors changed simultaneously when the amorphous TiO_2 is calcined. By phase transition anatese and rutile are obtained. The band gaps are determined by the crystal structure, even if the composition is the same. This fact is evidenced by the fact that anatese have a band gap of 3.2 eV while rutiline has 3.0 eV. This band gap differences is caused by the difference in the level of conduction band that leads materials to have variable photocatalytic capabilities [33].

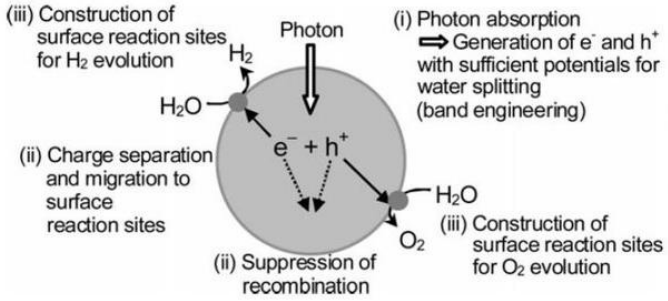

Figure 1.2 Photocatalytic water splitting process[29]

Calcination is a favourable factor that increases the crystallinity (Figure 1.3).However an increased particle size decreases the surface area through sintering which is obviously a adverse factor. Sometimes an inverse relationship can be seen between grain size and band gap. Smaller the grain size causes the broadening of band gap which in turn causes absorption in lower wavelengths. The balance among these factors dominates the resultant photocatalytic activity. As recombination between photo generated electrons and holes is especially a serious problem for uphill reactions. To split water, high degree of crystallinity is required instead of a large surface area. Not with standing high surface area is required for photocatalytic degradation of organic compounds for the adsorption of the organic compound is the important process. Photocatalytic activity may also be affected by the concentration of surface hydroxyl groups [29, 34].

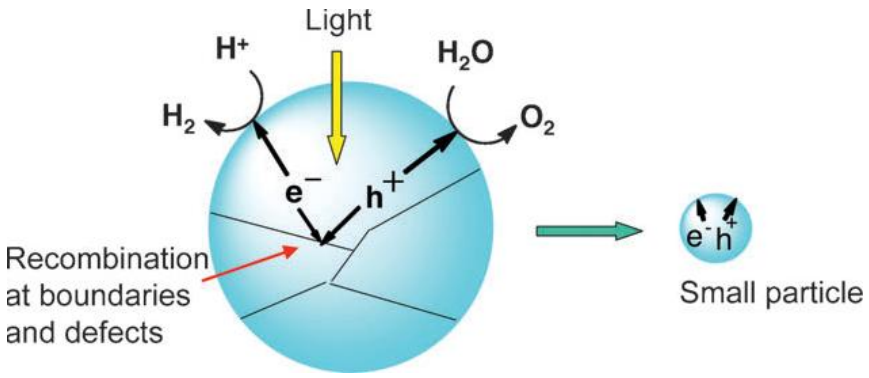

Figure 1.3 Effects of grain size and boundary on photocatalytic activity [29]

Most photocatalysts can also be materials for solar cells, dielectrics and phosphors. Yet, photocatalyst and other materials are very different from each other: While the photocatalytic process involves chemical reactions, it does not include physical properties. These photocatalytic activities can be obtained under the condition that these 3 steps simultaneously completed. Therefore surface properties suitable bulk and energy structure are essential for photocatalysts which demonstrates why the photocatalysts should be highly functional materials [35].

1.5 $Cd_xZn_{(1-x)}S$ Photocatalysts and Production Methods

Photocatalysts have a significant place for hydrogen production. An ideal photocatalysts for photocatalytic hydrogen production has the following characteristics [25, 36, 37]:

- for the absorption of extreme solar radiations with the assistance of narrow band gap along with high light absorption
- sufficient active reaction sites,
- efficient separation and migration of photo-induced electrons and holes,
- high activity,
- high stability,
- lower band gap
- band gap energy larger than the water oxidation potential,
- more negative conduction band edge than standard H_2 reduction potential.

Cadmium sulphide (CdS) ensures that it is a suitable photocatalyst to produce hydrogen from water under irradiation of visible light, with a suitable transmission band (CB) position and a direct and narrow band gap (2.4 eV)[38, 39].

CdS gives a strong response to visible light because ofsp^3 orbital of the valance band have a higher level of energy[40, 41].

However, there are some limitations the wide application of CdS. Under visible light, CdS undergoes high photo corrosion. Moreover, charge carriers which are photo generated in CdS recombination quickly. These problems directly affect the photocatalytic activity of CdS and the stability during photocatalysis reactions[42, 43].To overcome these problems, researchers have been tried to improve CdS activity as a photocatalysts by controlling conduction and valance band positions[44]. For this reason, designing CdS with other semiconductors which have a wide gap band and inserting CdS particles into layered compounds are tried. Moreover, investigations have been focused on designing CdS by doping with co-catalyst and adapting the particle size [45-47]. Studies show that the photocatalytic activity of non-catalyzed photocatalysts is very high while included catalysts exhibit higher performance.

Besides, zinc sulfide (ZnS) is another candidate of an efficient photocatalyst to generate hydrogen. The ZnS has a wide band gap value with 3.6 eV thanks to its high conduction band position. Having this wide band gap makes it impossible for ZnS to utilize the visible light irradiation. As a result, ZnS only expose a high photocatalytic activity under ultraviolet light. By doping various transition metal cations including Pb, Cu, Ni and Sr, ZnS absorbance in the visible region is tried to increase [38, 42, 48, 49].Cadmium zinc sulfide solutions ($Cd_xZn_{(1-x)}S$) became one of the most attractive photocatalysts due to the fact that their band gaps can be controlled and they are a good corrosion-resistant .Since $Cd_xZn_{(1-x)}S$ is composed of both CdS and ZnS, it is possible to control width and position of band gap by changing Cd/Zn. To achieve higher photocatalytic activity and better quantum yield, approaches for modification of CdZnS is required. $Cd_xZn_{(1-x)}S$ photocatalyst is also a good resistance for photo corrosion[50, 51].

$Cd_xZn_{(1-x)}S$ possesses the higher CB and VB, more photo-stable, and having the higher absorption of solar radiations in UV and visible region has remarkably higher hydrogen production rate [3, 44]. It is known that synthesis method of photocatalysts also affects the activity. Therefore, to enhance photocatalytic activity, several methods have been explored including hydrothermal [52, 53], co-precipitation [39], chemical bath deposition [54], cation exchange[55], thermolysis [56], micro-emulsion [57]and novel thermal sulphirization[58].

For thermal sulphurization, $Cd_xZn_{(1-x)}S$ particles generally synthesized with zinc acetate dihydrateand cadmium acetate dihydratemixture with H_2S gas[58]or aqeous precipitation of

Cd^{+2} and Zn^{+2} mixture with S^{2-} /SO_3^{2-} [44, 59-61]. Zhang and his coworkers prepared the $Cd_xZn_{(1-x)}S$ particles by thermal sulphurization method of zinc acetate dihydrateand cadmium acetate dihydratemixture with H_2S gas. He reported that thermal sulphurization method enhances the photocatalytic activity of $Cd_xZn_{(1-x)}S$ in comparison with conventional co-precipitation method with and/or without thermal treatment. Likewise, D. Jing et. al synthesized Pt loaded-CdS particles by the same method .However, utilizing H_2S as a sulphur source also has drawbackslike difficulties of the toxicity of H_2S gas and reaction control. To overcome such problems, in our previos work we have developed a new thermal sulphurization procedure by using elemantal sulphur[62].

1.6 Principle of Characterization Techniques

In this section, X-ray diffractometer (XRD), scanning electron microscopy (SEM) and UV – visible diffuse spectroscopy, energy-dispersive X-ray spectroscopy (EDS) and Raman spectroscopy techniques which are practiced during experiment will explain in detail.

1.6.1 X-Ray Diffraction

XRD technique is used for the identification of the crystal structure. It also provides information about atomic spacing. By this technique, unit cell parameters, positions of various atoms in crystal structure, structural parameters such as strain and grain size can be determined. The basis of this method is to reflect the x-rays of electromagnetic waves having very short wavelengths over the sample for analysis and distortion to the atoms of the crystals.

XRD is used for crystal structure determination due to the following reasons:

- The wavelengths of the X-rays are in the atomic distances of condensed material.
- X-ray scattering techniques do not lead to deterioration of the sample.
- Even small amounts of samples are sufficient for analysis.

The working principal of XRD is based on the idea that every crystal possess its own unique characteristic atomic sequences which deflect/break the incident X-rays in that respective order. There are three main parts of x ray diffractometers; x ray detector, x ray tube and sample holder. x ray tube which are given in Figure 1.4. [64].

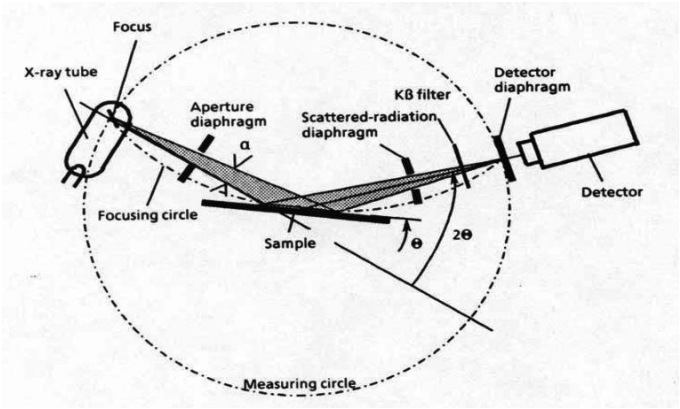

Figure 1.4 Diffractrometer system diagram [64]

X-rays are absorbed by electrons when they come onto crystal. Then, electrons begin to oscillate. These oscillating electrons emit x-rays photons in all directions by acting as an x-ray source. These photons scattered from different parts of the crystal form a measurable x-ray intensity [65].

Firstly, cathode ray tube generates x rays. Then, the rays are filtered to produce monochromic radiation and collected to concentrate. Finally, these rays are sent to the sample. The availability of conditions for Bragg's Law allows constructive inference to occur. X rays interact with the sample reveals constructive inference.

Bragg's Law explains crystalline diffraction of x-rays. X rays are reflected when they are transferred to atomic planes parallel to each other. Due to the difference in distance between neighbouring crystal planes, two different beams travel different lengths. Bragg's Law gives the relationship between the distance (d) between the crystal planes and the diffraction angle (θ) which is between the crystal planes and scattered electron beam. For the formation of constructive interference, the difference in the path between the scattering of different planes must be equal to the full lengths of the wavelength. This is called the Bragg Diffraction .According to the Figure 1.5, 2θrepresents the angle between incoming and scattered beam[66].

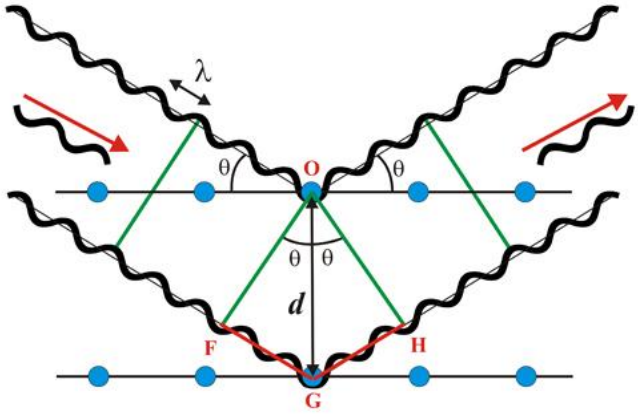

Figure 1.5 Bragg Diffraction [66]

$$|GH|=d\sin\theta \quad (8)$$

$$|FG|=d\sin\theta \quad (9)$$

$$|GH| +|FG|=2d\sin\theta \quad (10)$$

$$n\lambda=|GH| +|FG| \quad (11)$$

$$n\lambda=2\theta d \quad (12)$$

Bragg's Law is valid only when $\lambda \leq 2d$. As it is not possible to provide this condition with visible wavelength, X rays are used [67].

1.6.2 Scanning Electron Microscopy

SEM is a system which provides high resolution images from the sample surface using electrons. SEM is an effective technique to determine the three-dimensional images of the sample surface.

The image in the scanning electron microscope (SEM) is obtained by sample amplifiers from various sources after passing through a cathode ray tube, focusing on the sample during scanning of the electron on the sample surface. Interactions between the effects of the appropriate sensors and the signal amplifiers are transmitted to the screen [68, 69].

First of all, from the filament, an electron beam is produced by electron gun. In general, the electron gun used is a tungsten hairpin gun with a filament in the form of a tungsten coil that acts as a cathode. The voltage supplied to the windings results in heating. Then,

anode will create a force that can pull the electrons forward towards the anode. The magnetic lens focuses on electrons at a point on samples surface. Focused electron beam scans the entire sample guided by the scanner coil. When electrons hit the sample, electron scattering occurs. From the sample surface, both the Secondary Electron (SE) and the Back Scattered Electron (BSE) occur. Then, dedector detects these electrons and these electrons are shown as a CRT monitor. SEM does not require thinned samples, so it can be used to view objects from a 3D perspective [70-72].

There are many important signals produced by SEM. In Figure 1.6, the electron beam-sample interaction is given.

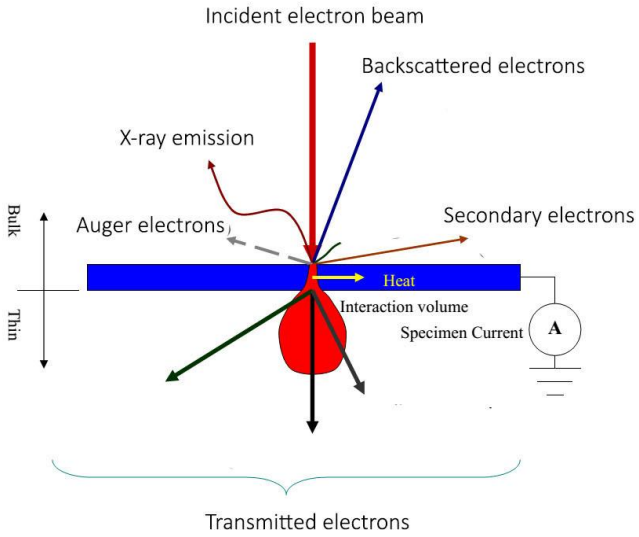

Figure 1.6 Electron beam-sample interaction[73]

Secondary electron signal and X-ray characteristics are obtain from non-elastic reflection whereas back scattering electron signal is obtained from elastic scatter. With the help of x-ray characteristic, chemical information about the emitting atoms can be obtained. Besides, for imaging, SE and BSE are utilized. These signals are described as follows.

As a result of collision between the atoms nuclei in the sample examined and incoming electrons, the back-scattered electrons are formed. The larger the atomic number of the atoms in the sample, more BSE are obtained. The energetics of the electrons in the elastic collision is very small.

Secondary electrons are caused by non-elastic collisions between incoming sieves and weakly bound electrons or valence electrons in the conductivity band. Thus, the electron from the examined sample is ruptured.

Secondary electrons are low energy electrons. They can easily be collected by applying a positive voltage of 100-300 V to the detector. In this way, 50-100% of the secondary electrons can be collected. Thus, 3-D view of the examined region is obtained [68, 74, 75]

SEM consist of five elements: electron gun, magnetic lens, dedector, sample holder and cathode ray tube [76, 77].

I. Electron Gun

They are sources that produce enough electron to concentrate on the sample. Electron guns are categorized into 3; Tungsten, field emission electron gun (FEG) and lanthanum hexaboride.

Tungsten electron gun: In this welding, the tungsten wire is bent to give a fine tip shape so that the diffusion surface is too small. The filament becomes hot with the current passing through it. It heats up until 2700 °C. It needs 10^{-3} Pa working vacuum.

Lanthanum Hexaboride (LaB_6) electron gun: It is created by placing the crystalline LaB6 on Tungsten or Rhenium. When the voltage is applied, the crystal heats up and starts emitting electrons. It operates at low temperatures. It resists high currents.

FEG electron gun: The FEG pistol has a tungsten-zirconium tip. It has the best resolving power and performance. Electrons are drawn from the wire in high vacuum and high magnetic field effect. This gun does not have heating. The resolution is 1/10 of the tungsten electrode and 1/5 of the LaB_6. The life span is 1000 times higher than that of Tungsten filament [77, 78].

II. Magnetic lens

The magnetic lenses used are two concentrator lenses. The second lens capacitor focuses the electrons with a very small diameter around 10-20 nm [68, 79].

III. Dedector

SEM has many detectors that perform the function of capturing electron scatter and providing different information. Dedector includes; backscatter detector that functions to capture information about atomic numbers and topography and secondary detector for information about topography.

IV. Sample holder

Sample holder is where the samples are analysed by SEM

V. Cathode ray tube

The image of an enlarged material structure can be seen on this cathode ray tube screen.

1.6.3 UV-VIS Diffuse Reflectance Spectroscopy

If the variance in energy difference between the basic state and the excited state is smaller than or equal to the energy of the beam to be absorbed, then the adsorption occurs. UV-Vis diffuse reflectance analysis is the characterization method that measures the absorbance, reflectance and transmittance ability of materials. Each molecule can absorb or reflect light at different wavelengths. Since the different materials have different molecular, atomic and molecular space structures, the absorption of light energy is also different [80-82].

When the beam is absorbed in visible region or UV region of the electromagnetic radiation, these high energy rays stimulate the bond electrons in the molecule. These stimulated particles are from a low energy state (basic state). They pass through a higher-energy state which is also called as excited state to absorb a photon from the beam coming from an electron semiconductor and pass through the VB) to the CB. The energy of the photon to be equal to or greater than the energy gap (Eg) [83].

The UV-Vis spectrophotometer is based on the principle of stimulating bond electrons by absorption or reflectance occurring in the material Absorption or reflectance spectra show bands corresponding to structural groups within the molecule. In reflectance measurement, lower reflectance values corresponds the stronger absorbance. The wavelengths of the reflectance peaks seen in spectroscopy are used to determine the band intervals of the materials [83-85].

As band gap is a characteristic feature that determines the application of material, powder samples band gap can be determined easily by using UV-vis reflectance spectra.

Kubelka Munk theory defines the diffuse reflectance spectra. Therefore, this theory can be used to analyse diffuse reflectance spectra. According to the Kubelka-Munk theorem, the reflectance properties are related to the ratio of absorption to the scattering coefficients and these values are two constants. It pretends there is no specular reflection [86-89].

Specular and diffuse reflections can be seen Figure 1.7. Reflection angle and incidence angle of specular reflection which is denoted by shaded arrows are equal to each other. On the contrast, for diffuse reflections, angle of reflection is independent of the angle of incidence.

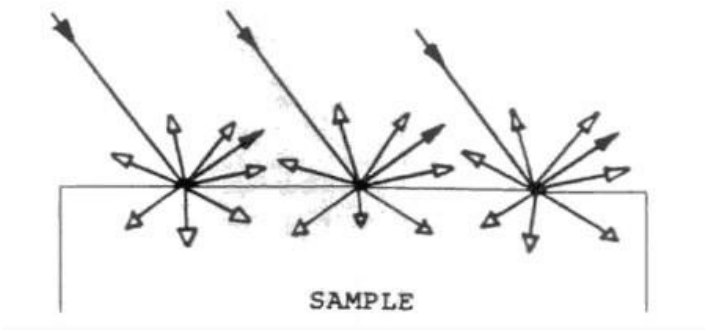

Fig 1.7 Specular and Diffuse reflections [86]

A UV-Visible spectrophotometer includes a light source, a monochromator (wavelength selector) and detector. The optical signal is transformed into the dedectors electrical signal. This process is recorded with the help of galvanometer. For electronic spectrum; ranges are between 100 and 700 nm, for vacuum UV; ranges are 100 and 200 nm. Between 200 and 400 nm represents the UV whereas visible regions ranges are between 400-700 nm[90].

1.6.4 Raman Spectroscopy

Light scattering is formed as the molecules interact with an intense monochromatic beam, only if the absorption of light does not take place during the interaction. The energy of a huge part of the light which is scattered during this interaction is equivalent to the energy of light that interacts with the matter. This scattering defines Rayleigh's scattering and can be categorized as elastic. Besides, only in a small quantities of non-elastically light scattered which is named Raman's scattering. During Raman scattering, redundancy or lack of light in the energy of light scattered during Raman scattering is as much as the energy difference between the light energy of the molecule interacting with the light. Therefore, the spectroscopic examination of Raman scattering also allows the knowledge on molecules energy levels [91].

The wavelength of the light interacting with the molecule and the wavelength of the scattered light are different to each other. These differences create a Raman shift and these shifts give information about the structure of the molecule. Obtained Raman shifts are the direct measurement of the vibration energies of molecules.

The quantum definition of Raman scattering is shown in the Jablonski energy diagram. (Figure 1.8) This diagram describes Raman scattering as quantum mechanics. If the energy of

the beam source to be used is not energized enough to induce the molecule from the basic state, the electrons are stimulated to the virtual state between the molecules basic state and the lowest electronic excited state [92].

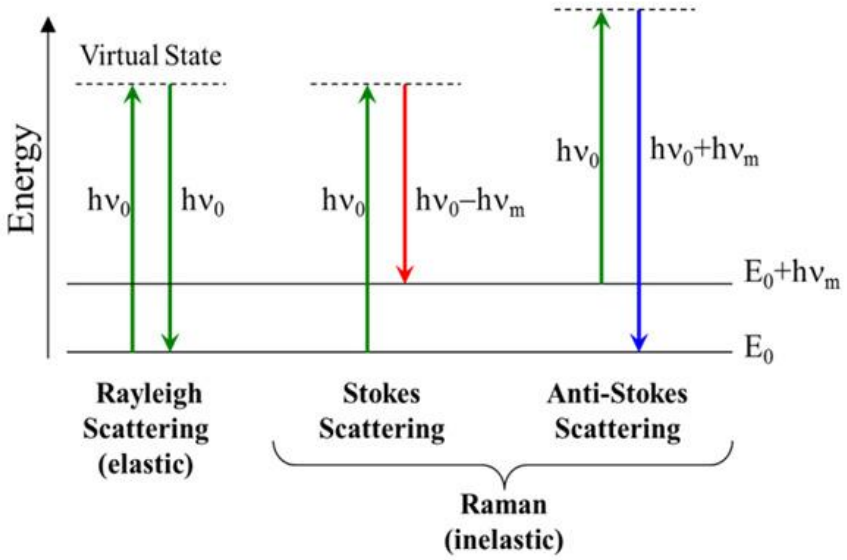

Figure 1.8 Jablonski energy diagram for Rayleigh and Raman scattering[93]

During the collision, if the photon gains an energy hvm, the photon is scattered at hv0-hvm frequency. This fact is called Stoke Raman scattering. On the other hand, for Anti-Stokes Scattering, the photon loses some energy and scattered at hv0+ hvm frequency.

If some of the sent photons energy is transferred to the molecule, Stokes lines occur whereas if energy is flowed from the molecule through the photon, Anti Stokes lines occur. Rayleigh's energy is the same as the energy of the light used. The energy of Stokes scattering is lower than the light used, while the anti-Stokes scattering is high [92, 94].

Raman spectroscopy which is a vibrational technique analyses the vibrations in the molecule. It is used to characterize a crystalline structure. It also can be used in analysis, quantification, and detection of contaminants since it ensures information about the sample examined with well-defined fingerprint bands.[95]. Each molecule or crystal has its own Raman spectrum. Raman spectroscopy uses the light emitted from the molecule detected in the Raman experiment to irradiate the sample as a single frequency source [96].

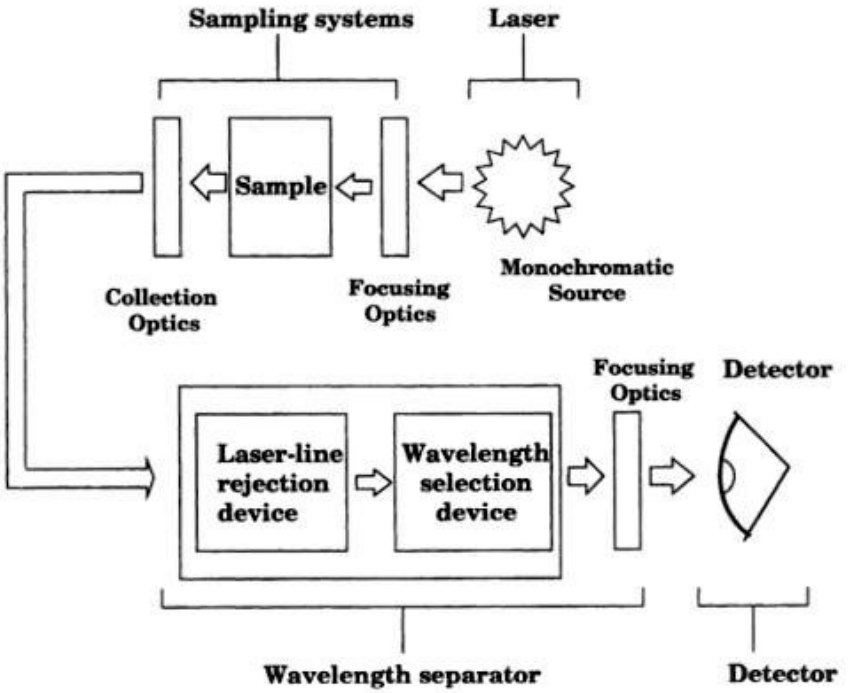

Figure 1.9 Block diagram of Raman spectrometer [96]

2 MATERIAL AND METHODS

2.1 Production of Photocatalysts

$Cd_xZn_{(1-x)}S$ and RGO- $Cd_xZn_{(1-x)}S$ photocatalysts preparation is consist of 3 parts. Firstly, reduced grapheme oxide was synthesized. Then, metal oxides were produced by thermal decomposition of the respective acetates. In the final step, $Cd_xZn_{(1-x)}S$ and RGO-$Cd_xZn_{(1-x)}S$ composites are obtained by thermal sulphurization.

2.1.1 Production of graphene oxide (GO) and reduced graphene oxide (RGO)

Graphene oxide (GO) was obtainedfrom Hummer's method [97]. In brief, 3.0 g of graphite powder were dissolved in 23.0 ml of concentrated H_2SO_4 using a magnetic stirrer in ice bath. After dissolution, 9 g of $KMnO_4$ was putinto the solution gradually. For stirring purpose, a sand bed was used and mixture was placed in the bedfor 30 minutes at 40° C. Then, 150.0 ml of purified water was added and the the temperature was maintained at 95° C for 15 minutes. After 500.0 ml of ultra pure water was added, 15.0 ml of a 30% H_2O_2 mixture was put into the solution and stirred during 2 hours. After the mixture was filtered, it was rinsed 3 times by the solution of 10% HCl. After drying for 12 hours at 50° C, graphene oxide is obtained as a black color powder.

By the reduction of GO by using hydrazine, reduced graphene oxide (RGO) was obtained. For the synthesis, 0.600 g GO and 300.0 ml pure water were placed in the bottom flask and mixed and placed in ultrasonic bath untill complete dissolution.

2 ml% hydrazine was poured into the solution and inthe presence of water-cooled condenser, heated untill 100˚C for 24 hours. Then, GO was converted to black solid and RGO was obtained. After the centrifuge, product was rinsed for 100.0 ml pure water and 100.0 ml methanol for 5 times. Finally, product was dried at the ambient temperature and RGO was obtained.

2.1.2 Production of Metal Oxides

For production of $Cd_xZn_{(1-x)}O$ and RGO-$Cd_xZn_{(1-x)}O$, zinc acetate dihydrate ($Zn(CH_3COO)_2.2H_2O$) and cadmium acetate dihydrate ($Cd(CH_3COO)_2.2H_2O$) were used as a cadmium and zinc source, respectively. By using different amount of cadmium acetate dehydrate and zinc acetate dihydrate, composition of $Cd_xZn_{(1-x)}S$ was arranged. Composition of catalysts synthesized by the use of Cd and Zinc in different ratios by weight is given in Table 2.1. These numbers are the values obtained from the pre-characterization calculations for the following mass weights.

Table 2.1 The amounts of chemicals used in thermal decomposition of photocatalysts having different weight ratios

Formula	Quantity of $Cd(CH_3COO)_2.2H_2O$ (gr)	Quantity of $Zn(CH_3COO)_2.2H_2O$ (gr)
$Cd_{0.3}Zn_{0.7}S$	0.474	2.680
$Cd_{0.5}Zn_{0.5}S$	1.499	1.230
$Cd_{0.7}Zn_{0.3}S$	1.365	1.423

During the thermal decomposition part, protherm tube furnace was used (Figure 2.1). The synthesis took place into the quartz tube. The one end of the tube was attached to the Argon gas supply while the other attached to a pipe placed in water filled beaker. Thus, the gas produced during the reaction was allowed to remain in the tube.

Figure 2.1 Protherm tube furnace

The temperature profile and scheme of the furnace tube was given in Figure 2.2.Oxidation process was taken place at 500 ˚C for 2 hours. The temperature value was adjusted to 500 degrees using the heater to remain constant. Argon gas was passed throughout the tube during the oxidation process.

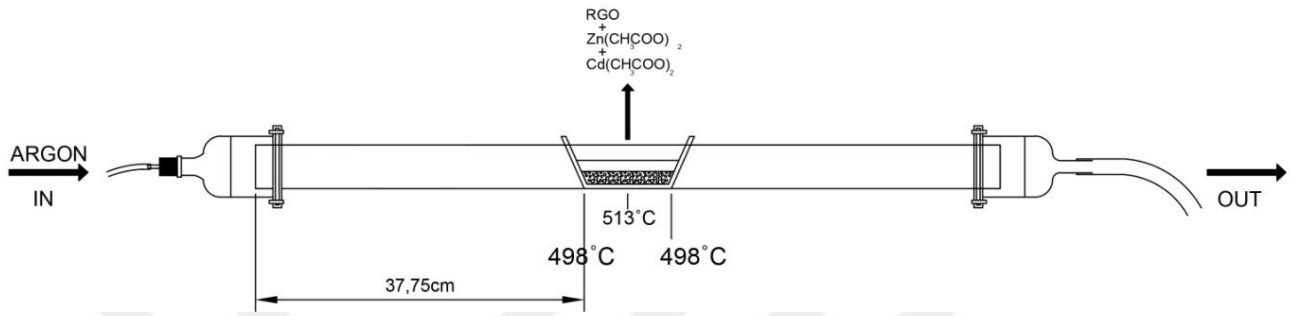

Figure 2.2 Scheme of the furnace tube

2.1.3 Production of Metal Sulfides

$Cd_xZn_{(1-x)}S$ and RGO-$Cd_xZn_{(1-x)}S$ composites are obtained by thermal sulphurization method. By using different amount of reactants, given in Table 2.1, composition of $Cd_xZn_{(1-x)}S$ was arranged. For this method, elemental sulphur was employed as a sulphur source. For metal sulfides synthesis, protherm tube furnace was used. The synthesis took place into the quartz tube. For RGO-$Cd_xZn_{(1-x)}S$ composites, required amount of RGO, $Cd(CH_3COO)_2$ and $Zn(CH_3COO)_2$ were placed in the same quartz cuvette, in the centre of the tube furnace. The synthesis took place into the quartz tube. For RGO-$Cd_xZn_{(1-x)}S$ composites, required amount of reactants were placed in the same quartz cuvette, at the middle of the tube furnace. Thermal sulphurization was carried out at 700 °C for 6 hours. Before sulphurization process, for the first half an hour of reaction, argon gas atmosphere was created with the continuous supply of gas. RGO- $Cd_xZn_{(1-x)}O$ was placed at the centre and sulphur was placed where the temperature corresponds to 200 ˚C. The same procedure was repeated for $Cd_xZn_{(1-x)}S$ photocatalysts at different ratios without RGO. The temperature profile of the tube, was such that 700 °C corresponds to the centre of the tube, whereas at 14 cm from the end of the tube temperature was almost 200 °C. Figure 2.3 depicts temperature profile of the furnace tube. RGO in $Cd_xZn_{(1-x)}S$ composites was optimised as %1.

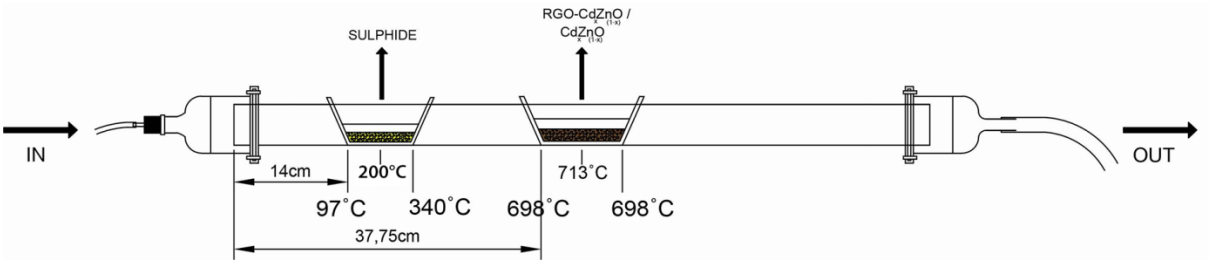

Figure 2.3 Temperature profile of the furnace tube

2.2 Characterization of Produced Photocatalysts

Crystal structure of the prepared photocatalysts was characterized with X-Ray diffraction. By scanning electron microscopy technique, particle size was determined and morphology was characterized. For band gap determination of photocatalysts, UV-VIS diffuse reflectance spectrometer was used. Chemical characterization of photocatalyst was analysed by using EDS technique. For the examination of molecular vibrations and crystal structures, Raman spectroscopy was employed.

2.2.1 X-Ray diffraction (XRD) analysis

It is well-known that crystal structure, size and morphology of the materials have a direct effect on the stability and activity of the photocatalyst. Therefore, to examine the crystal system of the samples, X-ray diffraction (XRD) structures were used. Bruker D2 Phaser X-ray diffractrometer under Cu Kα radiation at 10 ° <2θ <70 ° and with 1.5406Å wavelength was used to record XRD patterns for structure analysis.

2.2.2 Scanning electron microscopy (SEM) analysis

For the analysis of external morphology, orientation and composition of photocatalysts, SEM was used. SEM measurements were performed by using FEI Quanta FEG-450.

2.2.3 Energy-dispersive X-ray spectroscopy (EDS) Analysis

EDS was used at working range of 30 kV in 10.3 mm having secondary electron (SE) mode was used to analyse the chemical characterization of photocatalyst.

2.2.4 UV-vis diffuse reflectance spectra analysis

Band gap determination of the photocatalyst and understand the effect of RGO in light scattering, analysis is done by using PG instruments T92+ UV/VIS spectrophotometer in a range of 240-800 nm is used [98].

2.2.5 Raman Spectroscopy analysis

To provide information on molecular vibrations and crystal structures, Raman spectrophotometer STEX-100 was used.

2.3 Photocatalytic measurements

For photocatalytic measurements were performed by MAX-303 light source. Photocatalytic hydrogen production reactions took place into the quartz reactor. Asahi Spectra MAX-303 Xenon was used as a source of incident light during the photocatalytic hydrogen production measurements. For the analysis, 3.5 x 3.5 cm area was employed. Light source was adjusted in the manner that the source illuminates the whole surface area of catalyst locating at the base of reactor. For PC hydrogen production, certain amount of $Cd_xZn_{(1-x)}S$ (optimum amount was 700 mg) was suspended in Na_2S/Na_2SO_3 mixture of sacrificial reagent. Under the same reaction conditions, measurement of apparent quantum efficiency (AQE) was performed. Light source was adjusted to 3.33 Wm^{-2} at 460 nm. The following equation was used to calculate the AQE [99]:

$$\text{AQE } [\%] = \frac{\text{number of reacted electron}}{\text{number of incident photons}} \text{x} 100 \tag{13}$$

$$= \frac{\text{number of } H_2 \text{ molecules x } 2}{\text{number of incident photons}} \text{x} 100 \tag{14}$$

3 RESULTS AND DISCUSSIONS

3.1 XRD Analysis

For crystal phase investigation of samples, powder X-ray diffraction (XRD) structures was used .XRD analyses of the synthesized photocatalyst samples ($Cd_{0.3}Zn_{0.7}O$, $Cd_{0.3}Zn_{0.7}S$, RGO-$Cd_{0.3}Zn_{0.7}O$, RGO-$Cd_{0.3}Zn_{0.7}S$,$Cd_{0.5}Zn_{0.5}O$, $Cd_{0.5}Zn_{0.5}S$, RGO-$Cd_{0.5}Zn_{0.5}O$, RGO-$Cd_{0.5}Zn_{0.5}S$, $Cd_{0.7}Zn_{0.3}O$, $Cd_{0.7}Zn_{0.3}S$, RGO-$Cd_{0.7}Zn_{0.3}O$, RGO-$Cd_{0.7}Zn_{0.3}S$) were performed.

In Figure 1a the XRD patterns of metal oxides and metal oxides having RGO were given. $Cd_xZn_{(1-x)}O$ particles consisted of two phase CdO and ZnO. In the XRD patterns of Figure 1, $Cd_{0.7}Zn_{0.3}O$ had a two more peaks besides the $Cd_{0.3}Zn_{0.7}O$ and $Cd_{0.5}Zn_{0.5}O$. It was also observed that $Cd_{0.7}Zn_{0.3}O$ had a more distinct peaks that the others. XRD measurement of the samples containing RGO showed the similar results as the samples without RGO. When compared to the samples having same Cd/Zn ratio without RGO, $Cd_{0.7}Zn_{0.3}O$ peaks shifted to lower angle whereas peaks of other samples shifted to higher angle position. Also, it was observed that the peaks broad.

XRD patterns of metal sulfides were given inFigure3.1b. From the Figure 3.1b, it can be seen $Cd_xZn_{(1-x)}S$ solid had a single phase. Since Cd and Zn atoms had similar chemical properties, they can easily make solid solution .Seven major peaks were observed in the XRD pattern of the $Cd_xZn_{(1-x)}S$ photocatalyst. The peaks at 25.52°, 28.79°, 37.47°, 44.87 °, 48.94°, 52.27° and 55.74°, two theta values represent planes of (1 0 0), (1 0 1), (1 0 2), (1 1 0), (1 0 3), (2 0 0) and (0 0 4), respectively. From the XRD patterns of $Cd_{0.7}Zn_{0.3}S$, the phase was identified as a hexagonal (Joint Committee on Powder Diffraction Standards (JCPDS) Card No. 00-040-0836). The minor peaks seem adjacent to the major peaks proved that between Cd and Zn atoms, there was still diffusion.

It was observed that as the Cd/Zn ratio increased, the peak intensity sharpened and broadened. Moreover, it can be seen that the peak intensity of photocatalysts decrease when the Cd/Zn ratio in $Cd_xZn_{(1-x)}S$ solution ratio increases. As Cd atoms in $Cd_xZn_{(1-x)}S$ affect the Zn atoms position, crystal phase also changes from cubic to hexagonal[100]. In this study, the produced photocatalysts belong to hexagonal crystal system.

These results resemble the other literature surveys. The characteristic peaks of RGO are seen at 23 ° and 42 °. With the presence of RGO, diffraction peaks shifted to the left when compared to photocatalysts without RGO.

By using equation of Debye-Scherrer, the size of crystallite are calculated [101]:

$$D = \frac{K\,\lambda}{\beta\,\cos\theta} \qquad (15)$$

Where average particle size represented by D in nm, crystallite shape factor by K,FWHM (full width at half maximum) by β, diffraction angle by θ in degree and the wavelength of X-ray by λ in nm.

Applying this formula, crystallite sizes of (1 0 1) reflection of $Cd_{0.3}Zn_{0.7}S$, $Cd_{0.5}Zn_{0.5}S$ and $Cd_{0.7}Zn_{0.3}S$ are 6.58, 2.70 and 1.80 nm, respectively whereas the crystallite sizes of RGO-$Cd_{0.3}Zn_{0.7}S$, RGO-$Cd_{0.5}Zn_{0.5}S$ and RGO-$Cd_{0.7}Zn_{0.3}S$ are 1.77, 1.76 and 1.28 nm. This is because it is supposed that particles with a high degree of crystallization and affect photocatalytic activity[42, 97, 100].

According to the results, crystallite size of RGO-$Cd_xZn_{(1-x)}S$ were smaller compared to $Cd_xZn_{(1-x)}S$ particles.

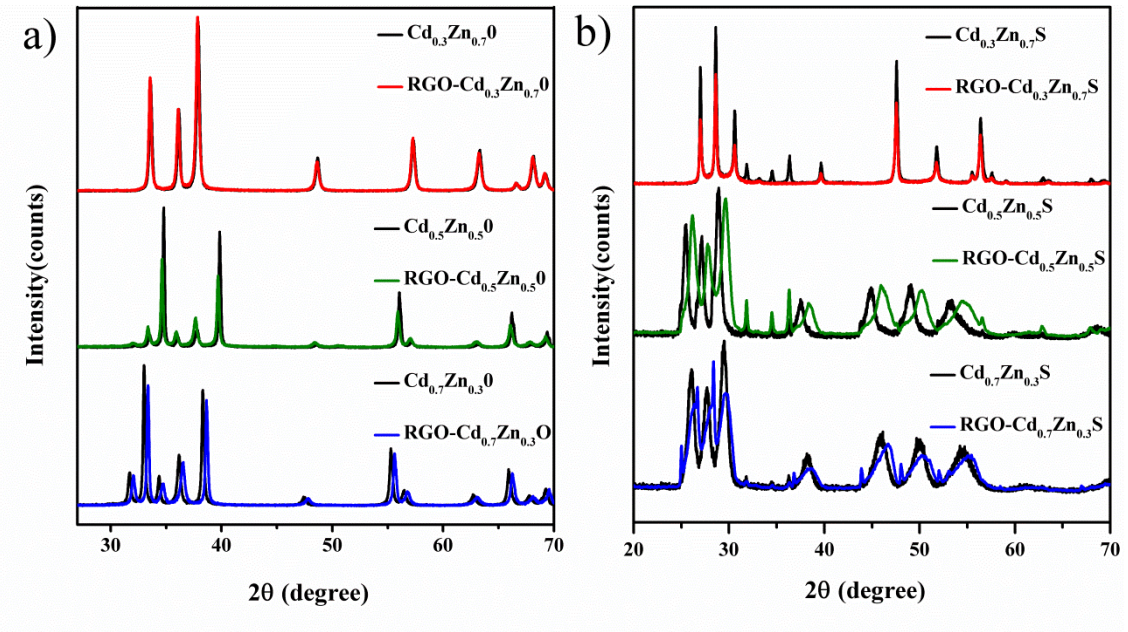

Figure 3.1 XRD patterns of a)metal oxides b)metal sulphides

In Figure 3.2, XRD patterns of RGO-$Cd_{0.7}Zn_{0.3}S$ after photocatalytic H_2 generation test was analysed and compared with the XRD patterns before usage for photocatalytic activity. It was observed that the peak positions did not change, shift and broaden. Lattice parameters are directly related to XRD peak positions, so any shift in the XRD peak causes the alteration in lattice parameters. The shift may also originate from the strain. Thus, the absence of a change

in peak position and peak width proves that there is no strain and composition change in powder photocatalysts. Also, it was not degraded by light and preserves the chemical structure.

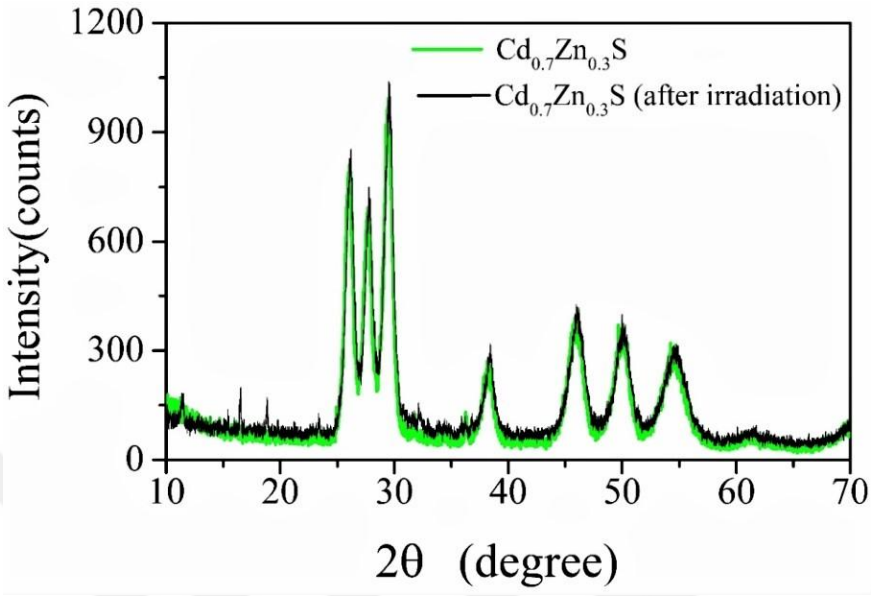

Figure 3.2 XRD analysis of RGO before and after photocatalytic H_2 generation test

3.2 SEM and EDS Patterns Of Photocatalysts

SEM images of both metal oxides and photocatalysts with RGO and without RGO were examined. When $Cd_{0.7}Zn_{0.3}S$ and RGO-$Cd_{0.7}Zn_{0.3}S$ are investigated, it was observed that the particles were dispersed and had a cabbage-like structure. According to the SEM results from Figure 3.3-3.4, particles have approximately 270 nm diameter. The existence of RGO has been proven by the cluster in the images can be seen from Figure 3.5 and 3.6. Moreover, it has been observed that the $Cd_xZn_{(1-x)}S$ particles ingrains in RGO layers properly. This fact shows us $Cd_xZn_{(1-x)}S$ particles are uniformly dispersed in RGO, thus decorating $Cd_xZn_{(1-x)}S$ particles with RGO prevents the aggregation.

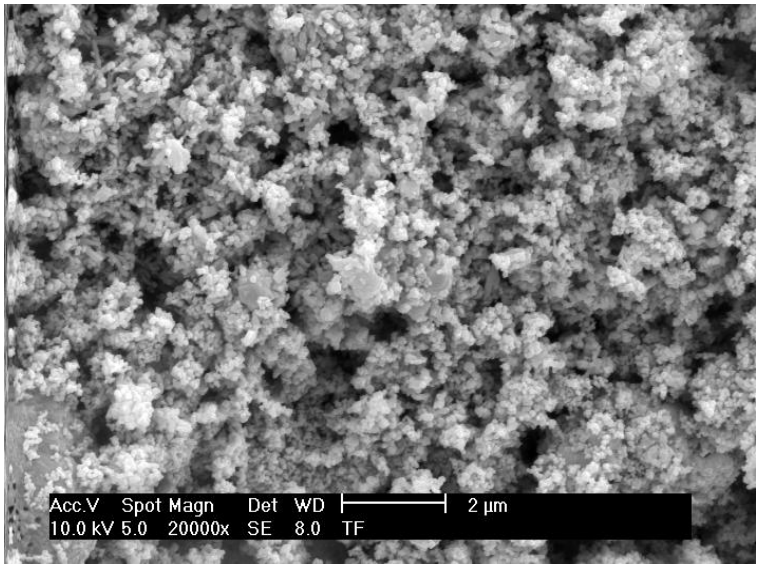

Figure 3.3 SEM image of $Cd_{0.7Zn0.3}O$ in 2000x magnification

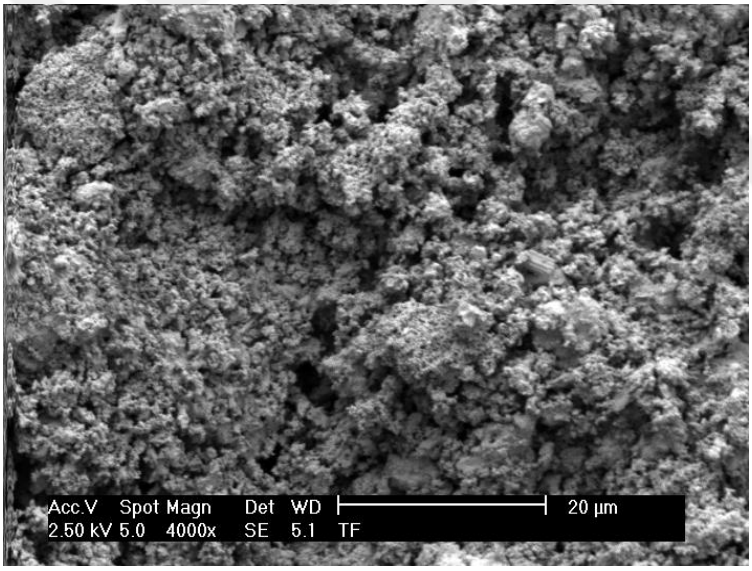

Figure 3.4 SEM image of $Cd_{0.7}Zn_{0.3}S$ in 4000x magnification

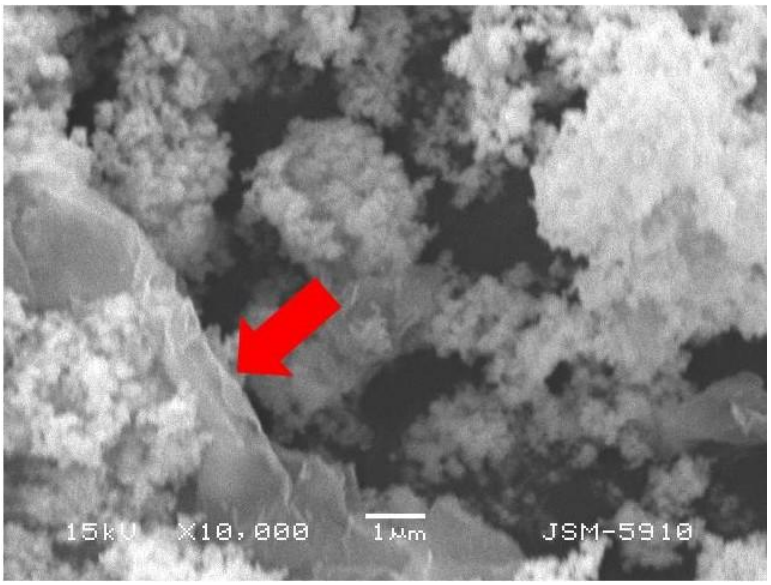

Figure 3.5 SEM image of RGO-$Cd_{0.7Zn0.3}O$ in 10000x magnification

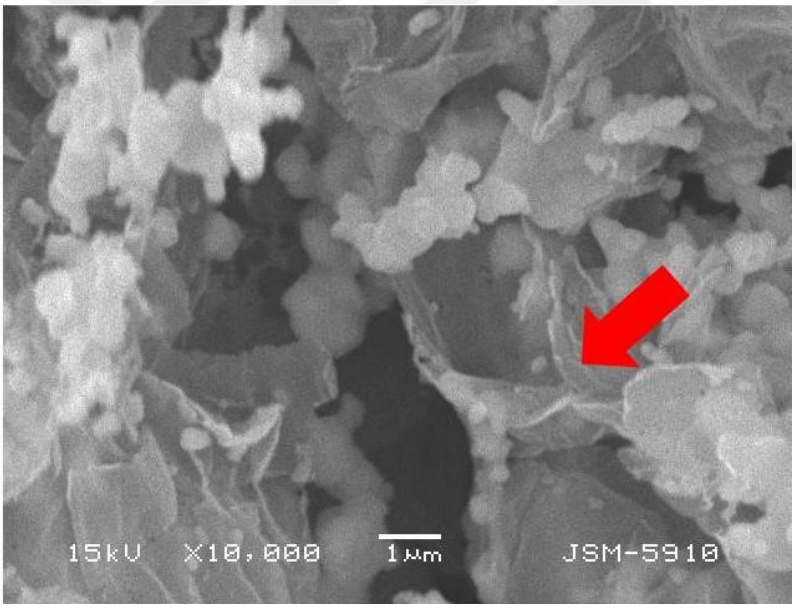

Figure 3.6 SEM image of RGO-$Cd_{0.7Zn0.3}S$ in 10000x magnification

Energy dispersive X-Ray spectroscopy is a powerful technique to examine the composition of potocatalysts. Identification of the elements and amount of these elements in $Cd_{0.7}Zn_{0.3}S$ were found by EDS technique. In Figure 3.6, results were given. Likewise, from Table 3.1 there were seen C, O, Cd, S and Zn atoms in $Cd_{0.7}Zn_{0.3}S$. Since reduced graphene oxide includes carbon atoms which were came from graphene, it is expected to exist carbon atoms. in RGO-

$Cd_{0.7}Zn_{0.3}S$ [102, 103]. Moreover, oxygen appearing in the EDS is evidence that the photocatalysts are oxidized.

Table 3.1.RGO-$Cd_{0.7}Zn_{0.3}S$photocatalyst by energy dispersive x-ray spectroscopy (EDS)

	RGO-$Cd_{0.7}Zn_{0.3}S$	
Elements	Wt %	At%
C	5.10	19.21
O	2.90	8.20
S	20.02	28.25
Cd	18.89	7.60
Zn	53.07	36.74
Total	100.00	100.00

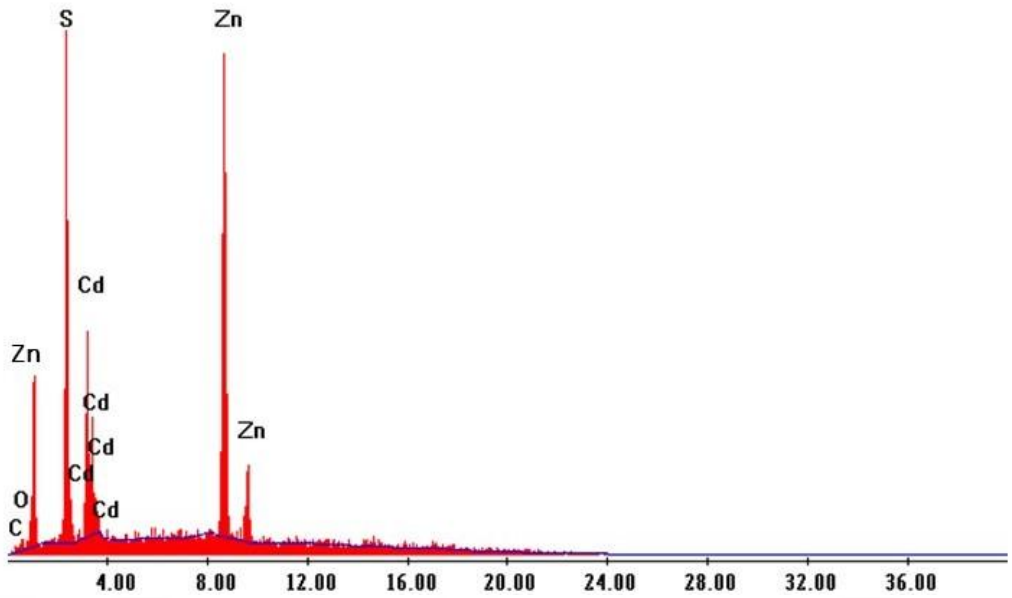

Figure 3.7 Energy dispersive X-Ray spectroscopy (EDS) patterns of RGO-$Cd_{0.7Zn0.3}S$

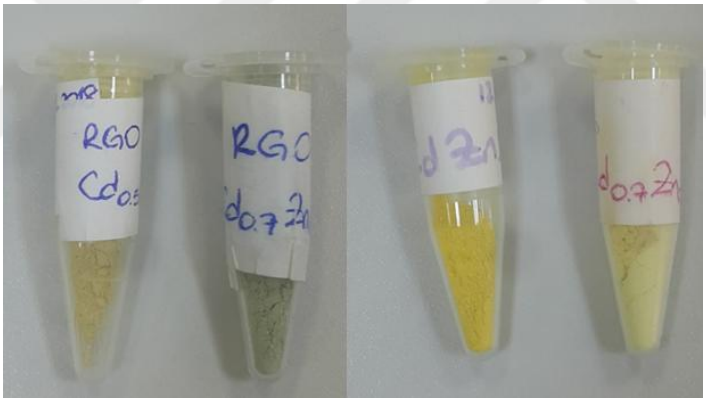

Figure 3.8 Appearance of produced photocatalysts after sulphurization method

In Figure 3.8, powder of $Cd_xZn_{(1-x)}S$ photocatalysts with different x values after sulphurization process can be seen. When the RGO is added in the photocatalysts, photocatalysts become darker, the colour changed yellow to green. This is explained by the presence of RGO in the photocatalysts.

3.3 UV-Visible Diffuse Reflection Spectra (DRS) Analysis

In Figure 3.9, the UV-vis diffuse reflectance spectra for solid $Cd_{0.7}Zn_{0.3}S$ and RGO-$Cd_{0.7}Zn_{0.3}S$ are given. According to the results, prepared photocatalysts' spectrum was found in visible light region (Figure 3.9a). From the Figure 3.9a, it can be seen that the $Cd_{0.7}Zn_{0.3}S$

photocatalyst decorated with RGO have a higher relative reflectance %R values than the without RGO. The wavelength of RGO-$Cd_{0.7}Zn_{0.3}S$ composite decreased shifting from 437 to 421 nm comparison with the $Cd_{0.7}Zn_{0.3}S$ composites in visible region. It can be postulated that the visible light utilization extent of RGO-$Cd_{0.7}Zn_{0.3}S$ photocatalyst would be enhanced, in comparison with that of $Cd_{0.7}Zn_{0.3}S$, because of the increase in light scattering property of RGO. Since RGO-$Cd_{0.7}Zn_{0.3}S$ utilize higher extent of visible light, it is more efficient for hydrogen production under visible light when compared to $Cd_{0.7}Zn_{0.3}S$.

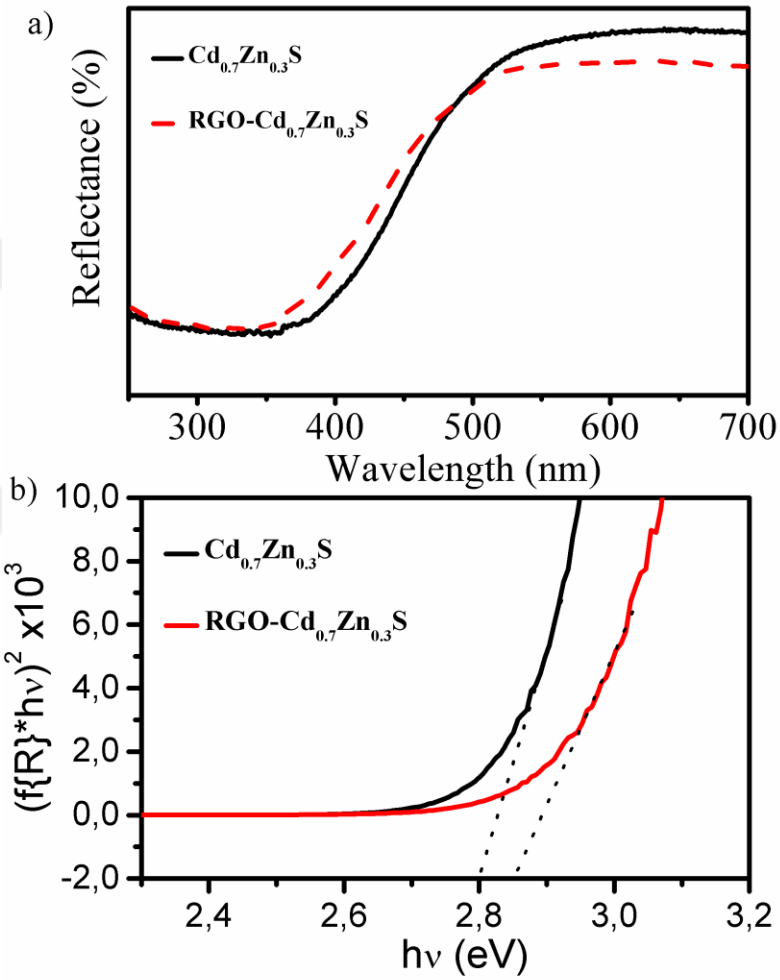

Figure 3.9 a) UV-visible diffuse reflectance spectra of photocatalysts $Cd_{0.7}Zn_{0.3}S$ and RGO-$Cd_{0.7}Zn_{0.3}S$ b) Kubelka-Munk function of Tauc-plot of photocatalysts $Cd_{0.7}Zn_{0.3}S$ and RGO $Cd_{0.7}Zn_{0.3}S$.

Band gap determination of the photocatalysts were done from the Kubelka-Munk function below [104]:

$$(h\nu F(R\alpha))^{1/n} = A(h\nu - E_g) \quad (16)$$

where photon energy represents by hν (ν is vibration frequency and h is Planck constant), absorption coefficient by α, direct band gap by Eg, reflectance by R and absorption coefficient (α) and F(R) is proportional to each other. A value and n value which is equal to 1/2 are the constant.

A plot of the Kubelka–Munk function of light energy $(f(R)h)^2$ versus energy (h) was also shown in Figure 3.9b. It was indicated that prepared solid photocatalysts had clear band gaps.

The band gaps of photocatalysts were calculated and from Table 3.2, band gap values can be seen. By varying Cd/Zn ratio not only conduction and valance band position, but also band gap can be easily controlled. The band gap values decreased when Cd/Zn ratio in photocatalyst increases. Among the $Cd_xZn_{(1-x)}S$ photocatalysts, the most narrow band gap value were found from $Cd_{0.7}Zn_{0.3}S$ having the maximum Cd/Zn ratio. This result is acceptable as the band gap of Cd is greater than that of Zn. However, there is no linear relationship between Cd / Zn ratio and band gap. Moreover, it is seen that the calculated band gaps were between the 2.4 and 3.6 eV which are the CdS bandgap and ZnS band gap [105-108].

On the other hand, as shown in Table 1, presence of RGO increases band gaps compared with the $Cd_xZn_{(1-x)}S$ composites. Since RGO has a higher band gap energy, $Cd_xZn_{(1-x)}S$ composites have generally the lower band gap values, when compared $Cd_xZn_{(1-x)}S$ particles including RGO. Furthermore, band gap affects directly to the photocatalytic performance. When the band gap increases, the higher energy is required as molecules must have more energy to exceed the band.

Table 3.2 Band gaps of $Cd_xZn_{(1-x)}S$ and RGO-$Cd_xZn_{(1-x)}S$photocatalysts

Photocatalyst	**Band gap**
$Cd_{0.3}Zn_{0.7}S$	3.05 eV
$Cd_{0.5}Zn_{0.5}S$	2.83eV
$Cd_{0.7}Zn_{0.3}S$	2.80 eV
RGO-$Cd_{0.3}Zn_{0.7}S$	3.20 eV
RGO-$Cd_{0.5}Zn_{0.5}S$	2.92 eV
RGO-$Cd_{0.7}Zn_{0.3}S$	2.86 eV

3.4 Raman Spectroscopy Analysis

Raman spectroscopy has been used to provide information on molecular vibrations and crystal structures for all photocatalyst including RGO-$Cd_xZn_{1-x}S$ composite powders at room temperature.

In Figure 3.10, Raman spectra of various $Cd_xZn_{(1-x)}S$ particles were given. According to the Raman spectroscopy, two major peaks were observed at 350 and 625 cm^{-1}. For each photocatalyst, longitudinal optical (1LO) mode was more strong than other one, overtone of LO mode (2LO). Due to the A1 mode of Cd-S bond vibration, approximately 300 cm^{-1} Raman peak was attributed to a CdS-like longitudinal optical mode (1LO) [109].Two more peaks can be seen for each RGO-$Cd_xZn_{(1-x)}S$ particles. These peaks were belong to D and G band. D band was formed approximately at 1300 cm^{-1} resulting from disordered sp^3 graphitic carbons whereas G band was formed at 1600 cm^{-1} due to the ordered sp^2 graphitic carbons. Presence of RGO was also proven by these bands. Among all particles, RGO-$Cd_{0.7}Zn_{0.3}S$ particles have the lowest intensity of not only B band but also G band. This can be caused by the fact that not all RGO are dissolved in $Cd_{0.7}Zn_{0.3}S$.

For RGO-$Cd_{0.5}Zn_{0.5}S$, it is observed that D and G bands overlap and one peak forms. Due to the overlap that can be attributed to the increased I_D/I_G ratio of GO after the reduction process, the removal of the oxygen moieties and the alteration of GO structure with an enhancement in the number of sp^2 domains [110].Moreover, RGO causes a shift in all peaks. These blue shifts can be properly seen from RGO-$Cd_{0.5}Zn_{0.5}S$ and RGO-$Cd_{0.7}Zn_{0.3}S$ in both 1LO and 2LO.

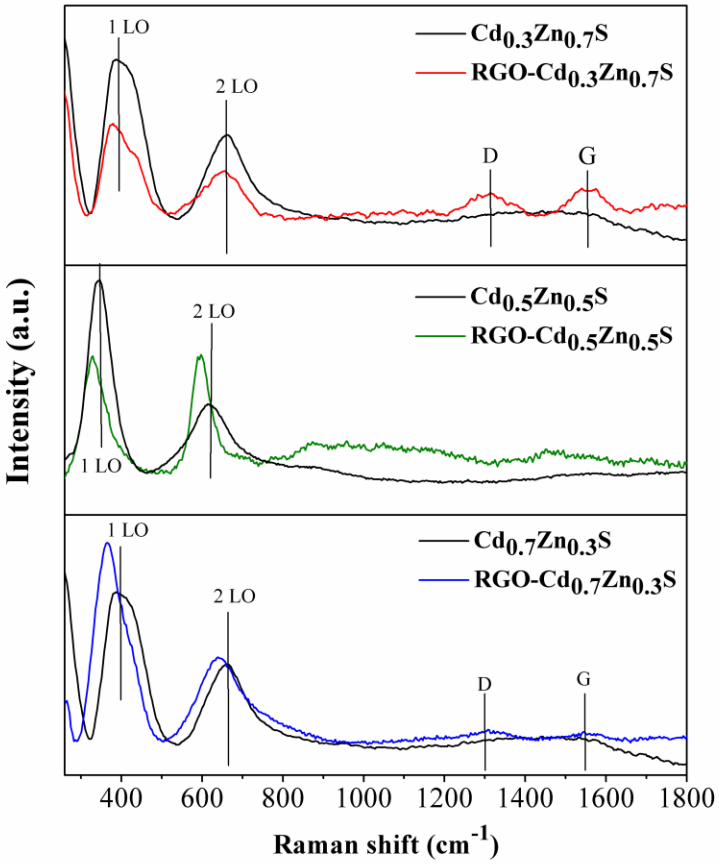

Figure 3.10 Raman spectroscopy of $Cd_xZn_{(1-x)}S$ particles

3.5 Photocatalytic H_2 Production Activity

Photocatalytic hydrogen evolution process can be described as follows. When the $Cd_xZn_{(1-x)}S$ nanoparticles are exposed to sunlight, the electrons (e^-) found on the valance band (VB) are excited to the conduction band (CB). This interaction leads to a formation of holes (h^+) in the valance band. Electron transfer on the conduction band is occurred owing to RGO. In consequence of reaction between electrons and adsorbed H^+ species, H_2 molecules are formed. For the sacrificial reagent, a mixture of Na_2S/Na_2SO_3 was utilized. S^{-2} ions which are generated by Na_2S is more unstable than the sulfide of photocatalysts. Na_2S is oxidized by photo excited holes. Then, S_n^{-2} ions are converted into S^{2-} ions in the presence of Na_2S [111, 112].

Photocatalytic hydrogen production was actualised by using light source and the photocatalytic activity of photocatalysts was tested. The system used for photocatalytic hydrogen production is given in Figure 3.11. The reason of using sacrificial agent during these experiments is to obtain only H_2 gas without O_2 gas. Since the oxidation potential of

SO_3^{-2} is lower than the potential of H_2O, during the photocatalytic reactions, only H_2 gas is produce as a product.

Figure 3.11 Photocatalytic hydrogen production system

In this system, particular amount of photocatalysts provided absorption of light. Thus, H_2 gas outlet took place. The volume of H_2 gas was measured from the liquid level difference in a burette by the replacement of hydrogen gas with liquid which was collected in a burette. Moreover, collected H_2 was found by gas chromatography.

Figure 3.12 exhibits the hydrogen generation of $Cd_xZn_{(1-x)}S$ with various concentrations. According to the obtained results, RGO-$Cd_xZn_{(1-x)}S$ samples had better photocatalytic activity than $Cd_xZn_{(1-x)}S$ samples. RGO-$Cd_{0.7}Zn_{0.3}S$ shows the remarkable photocatalytic activity in hydrogen production. In Table 3.3, all hydrogen production rates were given. These results were obtained by using a light intensity of 103 W/m^2.

Table 3.3 Hydrogen production rates

Photocatalysts	Hydrogen production rate ($\mu molh^{-1}$)
CdS	1.4
$Cd_{0.3}Zn_{0.7}S$	5.4
$Cd_{0.5}Zn_{0.5}S$	103.9
$Cd_{0.7}Zn_{0.3}S$	110.1
RGO-CdS	10.8
RGO-$Cd_{0.3}Zn_{0.7}S$	29.5
RGO-$Cd_{0.5}Zn_{0.5}S$	115.9
RGO-$Cd_{0.7}Zn_{0.3}S$	141.6

$Cd_{0.7}Zn_{0.3}S$ has the highest hydrogen production rate as 110.1 $\mu molh^{-1}$ in comparison with different concentration of Cd:Zn. Moreover, when Cd content in $Cd_xZn_{(1-x)}S$ increases, higher hydrogen rate is achieved. According to the literature, among the $Cd_xZn_{(1-x)}S$ photocatalysts, having Cd:Zn ratio of close to 0.7:0.3 have the highest hydrogen activity [113,114,115].

When the hydrogen rates were compared with RGO decorated $Cd_xZn_{(1-x)}S$, it can be seen that for all $Cd_xZn_{(1-x)}S$ particles including RGO have a better rate then the same photocatalysts having without RGO. RGO-$Cd_{0.7}Zn_{0.3}S$, achieving 1.3 times higher activity than $Cd_{0.7}Zn_{0.3}S$ alone. The highest amount of hydrogen production was found for RGO-$Cd_{0.7}Zn_{0.3}S$ which was approximately 141 6 $\mu molh^{-1}$ (1965 $\mu molh^{-1}g^{-1}$ for 1000 W/m^2).

Since RGO is a good electron acceptor, it transfer accepts and transfers the photo generated charge particles. Thus, RGO reduces the recombination of photo-excited electron-electron hole pairs. Moreover, another reason for photocatalysts have a better activity including RGO is that RGO increases the active adsorption sites and electron transfer rate under visible light.

The photocatalytic hydrogen production rate obtained by thermal sulphurization was higher than the $Cd_{0.7}Zn_{0.3}S$ photocatalysts obtained by different methods. For example, $Cd_xZn_{(1-x)}S$ photocatalysts obtained from this method is visibly higher than the same photocatalysts obtained from precipitation method [117]. Also, hexagonal structure of RGO-$Cd_{0.7}Zn_{0.3}S$ provides a better separation of electron hole pairs resulting a better hydrogen evolution efficiency and the highest apparent quantum efficiency was found as %19.4.

In the literature, photocatalytic hydrogen production by using RGO-CdZnS has not been done by using thermal sulphurization method.

Table 3.4 summarizes the photocatalytic hydrogen production activities of similar photocatalysts obtained by different synthesis methods. Since the synthesis method, co-catalyst addition and experimental conditions were not the same, direct comparison of these results was not correct, but these results allowed us to compare the method used in this study with others. The efficiency values given in the table can be used to evaluate the actual effect of reduce graphene oxide on the CdZnS photocatalytic performance for H_2 production. When the results compared to recent literature values, higher hydrogen rate and efficiency were observed in this study. During this study, it is aimed to enhance the efficiency by thermal sulphurization method.

Moreover, previous studies have also found that the presence of RGO increases photocatalytic activity [100, 111, 117]. Since the less photon absorbed than the incident light, calculated apparent efficiency value is estimated less than the real one [29].

The amount of hydrogen production was clearly higher than $Cd_{0.7}Zn_{0.3}S$ sample due to the ability of RGO to collect and transport for separating photo generated electron-hole pairs. It prevents photo corrosion and aggregation. Under visible light irradiation, it also plays a significant role in photocatalytic hydrogen evolution since it enhances the conductivity and decreases the size of particle by increasing the surface area.

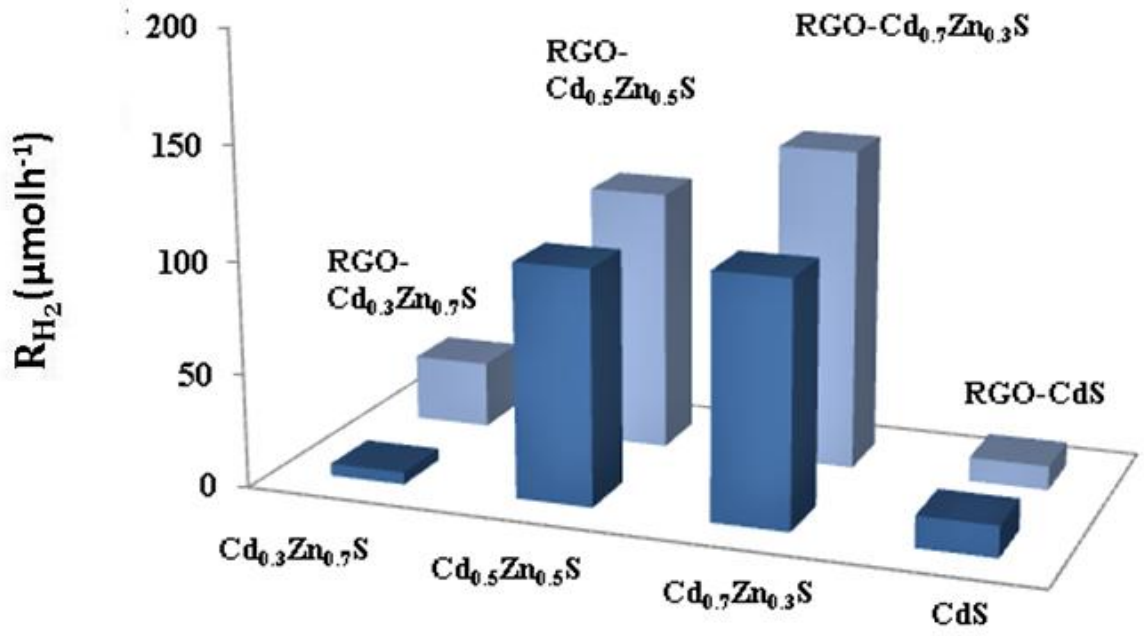

Figure 3.12 Under light irridation photocatalytic hydrogen production rates of synthesized photocatalyst samples (Reaction conditions: 700 mg of photocatalyst was dispersed in 0.25 M Na_2SO_3 and 0.35 M Na_2S and aqueous solution under Asahi Spectra MAX-303 Xenon light source at 1000 W/m^2).

There are several factors to increase the photocatalytic hydrogen production rate such as crystal size, crystallinity, crystal structure, light intensity and pH. By using thermal sulphurization method in this study, it is aimed to obtain better photocatalytic activity. Thermal sulphurization method provides a high temperature operation. This allows us to control the crystal structure, properties and morphology of the photocatalysts such as crystal size and band gap. In order to obtain better photocatalytic performance, firstly the parameters were optimized such as RGO amount, photocatalysts amount, weight ratio of Cd:Zn, light intensity, sulphurization temperature and period. The same concentration of sacrificial reagent was used this study since in our previous study the concentration of Na_2S/Na_2SO_3 was optimized as a mixture of 0.35 M and 0.25 M of Na_2SO_3. Moreover, RGO amount was optimized as %1. The highest hydrogen rate was obtained when 0.700 g of photocatalysts were used. As the hydrogen production rate depends on the activity of the active side of the photocatalyst that absorbs the light, not the total amounts of the photocatalyst, put more amount of catalyst did not increase the activity.

Table 3.4 A representative comparison of photocatalytic H_2 production activity from previous literature to present work of this work with related previous literature of the photocatalysts reported in recent literature.

Photocatalyst	Method	Sulphur source	Sacrificed agent	Light source	Co-catalyst	QE %	Rate of H_2	Stability	Ref.
RGO-$Zn_xCd_{1-x}S$	Hydrothermal	Thiourea	0.35 M Na_2S, 0.25 M Na_2SO_3	150 W Xe arc Lamp (140 $mWcm^{-2}$)	-	19.8	1060 $\mu molg^{-1}h^{-1}$	12 h	[118]
GO/CdS	Precipitation		0.35 M Na_2S, 0.25 M Na_2SO_3	300 W Xe-lamp, $\lambda \geq 420$ nm	-	4.8 (at 420 nm)	314 μMh^{-1}	-	[119]
CdS/RGO	Precipitation-Hydrothermal		0.35 M Na_2S, 0.25 M Na_2SO_3	300 W Xe-lamp, $\lambda \geq 420$ nm	-	-	70 $\mu molg^{-1}h^{-1}$	-	[120]
$Zn_{0.2}Cd_{0.8}S$	Chemical deposition	thioacetamide	0.35 M Na_2S, 0.25 M Na_2SO_3	$\lambda > 420$ nm (Xe) (100 $mWcm^{-2}$)	MoS_2	-	420 $\mu molg^{-1}h^{-1}$	-	[121]
$Zn_{0.3}Cd_{0.7}S$	Hydrothermal	sodium sulfide	10% lactic acid	$\lambda > 420$ nm (Xe)	MoS_2	-	1196 $\mu molg^{-1}h^{-1}$	6 h	[122]
RGO–CdS	Solvothermal	DMSO	0.35 M Na_2S, 0.25 M Na_2SO_3	300 W Xe-lamp, $\lambda \geq 420$ nm	-	10.4	420 $\mu molh^{-1}$	30 h	[123]
$Cd_{0.5}Zn_{0.5}S$	Co-precipitation	Na_2S	0.25 M Na_2S 0.35 M K_2SO_3	300 W halogen lamp (PHILIPS, Taiwan, l ¼ 400□ 1000 nm)	-	0.55 (30 º C) 1.29 (55 º C)	434 $\mu molh^{-1}$ (30 º C) 1019 $\mu molh^{-1}$ (55 º C)	50 h	[124]

$Cd_{0.8}Zn_{0.2}S$	Co-precipitation	Na_2S	0.25 M Na_2S 0.35 M K_2SO_3	300 W halogen lamp (PHILIPS, Taiwan, l ¼ 400□ 1000 nm)	-	0.35 (30 ° C) 0.69 (55 ° C)	274 μmolh^{-1} (30 ° C) 547 μmolh^{-1} (55 ° C)	50 h	[124]
CdS	Thermal sulfurization	Sulfur powder	0.35 M Na_2S, 0.25 M Na_2SO_3	Visible Light Simulator (1000 W/m^2)	-	-	1.4 μmolh^{-1}	-	This work
$Cd_{0.3}Zn_{0.7}S$	Thermal sulfurization	Sulfur powder	0.35 M Na_2S, 0.25 M Na_2SO_3	Visible Light Simulator (1000 W/m^2)	-	-	5.4 μmolh^{-1}	-	This work
$Cd_{0.5}Zn_{0.5}S$	Thermal sulfurization	Sulfur powder	0.35 M Na_2S, 0.25 M Na_2SO_3	Visible Light Simulator (1000 W/m^2)	-	-	103.4 μmolh^{-1}	-	This work
$Cd_{0.7}Zn_{0.3}S$	Thermal sulfurization	Sulfur powder	0.35 M Na_2S, 0.25 M Na_2SO_3	Solar Simulator (1000 W/m^2)	-	-	110.1 μmolh^{-1}	-	This work
RGO- CdS	Thermal sulfurization	Sulfur powder	0.35 M Na_2S, 0.25 M Na_2SO_3	Visible Light Simulator (1000 W/m^2)	-	-	10.8 μmolh^{-1}	-	This work
RGO-$Cd_{0.3}Zn_{0.7}S$	Thermal sulfurization	Sulfur powder	0.35 M Na_2S, 0.25 M Na_2SO_3	Visible Light Simulator (1000 W/m^2)	-	-	29.5μmolh^{-1}	-	This work
RGO-$Cd_{0.5}Zn_{0.5}S$	Thermal sulfurization	Sulfur powder	0.35 M Na_2S, 0.25 M Na_2SO_3	Visible Light Simulator (1000 W/m^2)	-	-	115.9 μmolh^{-1}	-	This work
RGO-$Cd_{0.7}Zn_{0.3}S$	Thermal sulfurization	Sulfur powder	0.35 M Na_2S, 0.25 M Na_2SO_3	Visible Light Simulator (1000 W/m^2)	-	19.4 (at 460 nm)	141.6 μmolh^{-1}	-	This work

4 CONCLUSIONS

In this study, $Cd_xZn_{(1-x)}S$ particles were modified with reduced graphene oxide (RGO) by thermal sulphurization method to develop the photocatalytic hydrogen production. As a result of this, $Cd_xZn_{(1-x)}S$ photocatalysts were produced by sulphurization of metal oxides corresponding metal acetates in tube furnace.

To investigate crystal structure, XRD technique was used. From XRD results, it was found that produced photocatalysts have a hexagonal crystal system and a single phase. This hexagonal structure provides a greater electron-hole pairs. Besides, better rate of hydrogen production is obtained. Moreover, as the Cd/Zn ratio increased, the peak intensity sharpened and broadened. This sharpness indicates high crystallinity. Crystallinity is also directly proportional to hydrogen activity. On the other hand, XRD peaks at the same point and intensity before and after irradiation prove that there is no strain and composition change in powder photocatalysts. The produced $Cd_{0.7}Zn_{0.3}S$ photocatalyst also is not degraded by light and preserve the chemical structure.

Three-dimensional images of the sample surface were analysed by SEM. It was observed that produced photocatalysts had a cabbage-like structure. According to the SEM results photocatalysts have approximately 270 nm diameter. The cluster in the SEM images is the proof of RGO existence. Moreover, it was observed that RGO interacted $Cd_xZn_{(1-x)}S$ particles properly. When EDS results of photocatalysts were examined, it is understood that the produced photocatalyst with highest efficiency is RGO-$Cd_{0.7}Zn_{0.3}S$ due to the existence of Cd, Zn, S and C atoms. Moreover, oxygen appearing in the EDS is evidence that the photocatalysts are oxidized.

Band gap is an important property for H_2 production, since it affects directly to the activity of photocatalysts. By using UV-VIS diffuse spectra, band gap values were determined. From the Kubelka-Munk function, band gap of $Cd_{0.3}Zn_{0.7}S$, $Cd_{0.5}Zn_{0.5}S$ and $Cd_{0.7}Zn_{0.3}S$ were found as 3.20, 2.90 and 2.85 eV respectively. These results prove that by varying Cd/Zn ratio not only conduction and valance band position, but also band gap can be easily controlled. The band gap values of produced photocatalysts are greater than CdS band gap and lower than ZnS band gap.

The molecular vibrations of the produced photocatalysts were characterized by the Raman spectroscopy. The formation of d band approximately at 1300 cm^{-1} resulting from disordered

sp^3 graphitic carbons and g band at 1600 cm^{-1} because of the ordered sp^2 graphitic carbons proves that there is RGO in the photocatalysts. For each photocatalysts, 1 LO and 2 LO was observed and longitudinal optical (1LO) mode was more strong than other one, overtone of LO mode (2LO).

Photocatalytic activity is affected by the crystal size, light intensity, crystal structure and crystallinity. Thus, for this study, the crystal size, band gap, amount of RGO and light intensity are optimised. Then, photocatalytic hydrogen activity of produced photocatalysts was investigated. Among all photocatalysts, RGO-$Cd_{0.7}Zn_{0.3}S$ has the highest hydrogen production rate of 141.6 $\mu molh^{-1}$. Likewise, it has the highest apparent quantum efficiency of %19.4. During the hydrogen production tests, RGO collects electron in a wide range and separates transport for separating photogenic electron hole pairs. It also enhances the conductivity. Thus, it was seen that photocatalysts with RGO has a better hydrogen activity. Moreover, sacrificial agents used during the test assist to increase the efficiency.

REFERENCES

1. Christoforidis, K.C. and P. Fornasiero, *Photocatalytic hydrogen production: a rift into the future energy supply.* ChemCatChem, 2017. **9**(9): p. 1523-1544.
2. Jafari, T., et al., *Photocatalytic water splitting—the untamed dream: a review of recent advances.* Molecules, 2016. **21**(7): p. 900.
3. Li, Q., et al., *Highly efficient visible-light-driven photocatalytic hydrogen production of CdS-cluster-decorated graphene nanosheets.* Journal of the American Chemical Society, 2011. **133**(28): p. 10878-10884.
4. Fujishima, A. and K. Honda, *Electrochemical photolysis of water at a semiconductor electrode.* nature, 1972. **238**(5358): p. 37.
5. Zini, G. and P. Tartarini, *Solar hydrogen energy systems: science and technology for the hydrogen economy*. 2012: Springer Science & Business Media.
6. Acar, C. and I. Dincer, *Comparative assessment of hydrogen production methods from renewable and non-renewable sources.* International journal of hydrogen energy, 2014. **39**(1): p. 1-12.
7. Shinnar, R., *The hydrogen economy, fuel cells, and electric cars.* Technology in society, 2003. **25**(4): p. 455-476.
8. Dincer, I. and C. Acar, *Review and evaluation of hydrogen production methods for better sustainability.* International journal of hydrogen energy, 2015. **40**(34): p. 11094-11111.
9. Kothari, R., D. Buddhi, and R. Sawhney, *Comparison of environmental and economic aspects of various hydrogen production methods.* Renewable and Sustainable Energy Reviews, 2008. **12**(2): p. 553-563.
10. Song, C., *Recent advances in catalysis for hydrogen production and fuel processing for fuel cells.* Topics in Catalysis, 2008. **49**(1-2): p. 1-3.
11. Squadrito, G., et al., *Advances in Hydrogen Production Storage and Distribution*, in *Hydrogen fuel cells technology*. 2014, Woodhead Publishing Limited.
12. Edwards, P., V. Kuznetsov, and W. David, *Hydrogen energy.* Philosophical Transactions of the Royal Society A: Mathematical, Physical and Engineering Sciences, 2007. **365**(1853): p. 1043-1056.
13. Dincer, I. and A.S. Joshi, *Solar based hydrogen production systems*. 2013: Springer.
14. Dincer, I. and C. Zamfirescu, *Sustainable hydrogen production options and the role of IAHE.* International Journal of Hydrogen Energy, 2012. **37**(21): p. 16266-16286.
15. Wei, R.-B., et al., *Dual-cocatalysts decorated rimous CdS spheres advancing highly-efficient visible-light photocatalytic hydrogen production.* Applied Catalysis B: Environmental, 2018. **231**: p. 101-107.
16. Momirlan, M. and T.N. Veziroglu, *The properties of hydrogen as fuel tomorrow in sustainable energy system for a cleaner planet.* International journal of hydrogen energy, 2005. **30**(7): p. 795-802.
17. Basile, A. and A. Iulianelli, *Advances in hydrogen production, storage and distribution*. 2014: Elsevier.
18. Ma, S., et al., *Noble-metal-free Ni3C cocatalysts decorated CdS nanosheets for high-efficiency visible-light-driven photocatalytic H2 evolution.* Applied Catalysis B: Environmental, 2018. **227**: p. 218-228.
19. Murphy, O. and B. JO'M, *Photovoltaic electrolysis: hydrogen and electricity from water and light.* International journal of hydrogen energy, 1984. **9**(7): p. 557-561.
20. Liao, C.-H., C.-W. Huang, and J. Wu, *Hydrogen production from semiconductor-based photocatalysis via water splitting.* Catalysts, 2012. **2**(4): p. 490-516.
21. Bolton, J.R., *Solar photoproduction of hydrogen. IEA technical report of the IEA Agreement of the Production and Utilization of Hydrogen*. 1996, ExCo Secretariat of the International Energy Agency Implementing Agreement ….
22. Nowotny, J., et al., *Solar-hydrogen: Unresolved problems in solid-state science.* Solar Energy, 2005. **78**(5): p. 593-602.

23. Getoff, N., *Photoelectrochemical and photocatalytic methods of hydrogen production: a short review.* International Journal of Hydrogen Energy, 1990. **15**(6): p. 407-417.
24. GRIMES, C., O. VARGHESE, and S. RANJAN, *Light, water, hydrogen: the solar generation of hydrogen by water photoelectrolysis*. 2007: Springer Science & Business Media.
25. Huang, J., et al., *Photodriven charge separation dynamics in CdSe/ZnS core/shell quantum dot/cobaloxime hybrid for efficient hydrogen production.* Journal of the American Chemical Society, 2012. **134**(40): p. 16472-16475.
26. Zhu, J. and M. Zäch, *Nanostructured materials for photocatalytic hydrogen production.* Current Opinion in Colloid & Interface Science, 2009. **4**(14): p. 260-269.
27. Chen, Z., et al., *Accelerating materials development for photoelectrochemical hydrogen production: Standards for methods, definitions, and reporting protocols.* Journal of Materials Research, 2010. **25**(1): p. 3-16.
28. Khan, S.U., M. Al-Shahry, and W.B. Ingler, *Efficient photochemical water splitting by a chemically modified n-TiO2.* science, 2002. **297**(5590): p. 2243-2245.
29. Kudo, A. and Y. Miseki, *Heterogeneous photocatalyst materials for water splitting.* Chemical Society Reviews, 2009. **38**(1): p. 253-278.
30. Gratzel, M., *Energy resources through photochemistry and catalysis*. 2012: Elsevier.
31. Nozik, A.J., *Photoelectrochemistry: applications to solar energy conversion.* Annual Review of Physical Chemistry, 1978. **29**(1): p. 189-222.
32. Mills, A. and S. Le Hunte, *An overview of semiconductor photocatalysis.* Journal of photochemistry and photobiology A: Chemistry, 1997. **108**(1): p. 1-35.
33. Tomita, K., et al., *A water-soluble titanium complex for the selective synthesis of nanocrystalline brookite, rutile, and anatase by a hydrothermal method.* Angewandte Chemie International Edition, 2006. **45**(15): p. 2378-2381.
34. Chakrabarti, S., *Solar Photocatalysis for Environmental Remediation*. 2017: The Energy and Resources Institute (TERI).
35. Ni, M., et al., *A review and recent developments in photocatalytic water-splitting using TiO2 for hydrogen production.* Renewable and Sustainable Energy Reviews, 2007. **11**(3): p. 401-425.
36. Zhu, H., et al., *Near unity quantum yield of light-driven redox mediator reduction and efficient H2 generation using colloidal nanorod heterostructures.* Journal of the American Chemical Society, 2012. **134**(28): p. 11701-11708.
37. Cao, S. and J. Yu, *g-C3N4-based photocatalysts for hydrogen generation.* The journal of physical chemistry letters, 2014. **5**(12): p. 2101-2107.
38. Chen, X., et al., *Semiconductor-based photocatalytic hydrogen generation.* Chemical reviews, 2010. **110**(11): p. 6503-6570.
39. Del Valle, F., et al., *Influence of Zn concentration in the activity of Cd1− xZnxS solid solutions for water splitting under visible light.* Catalysis Today, 2009. **143**(1-2): p. 51-56.
40. Sasikala, R., et al., *Cubic phase indium doped cadmium sulfide dispersed on zinc oxide: enhanced photocatalytic activity for hydrogen generation from water.* Applied Catalysis A: General, 2013. **464**: p. 149-155.
41. Kahane, S.V., et al., *CdO–CdS nanocomposites with enhanced photocatalytic activity for hydrogen generation from water.* international journal of hydrogen energy, 2013. **38**(35): p. 15012-15018.
42. Peng, Q.-X., et al., *Visible-light-driven photocatalytic system based on a nickel complex over CdS materials for hydrogen production from water.* Applied Catalysis B: Environmental, 2017. **219**: p. 353-361.
43. Li, Q., et al., *CdS/graphene nanocomposite photocatalysts.* Advanced Energy Materials, 2015. **5**(14): p. 1500010.
44. Chan, C.-C., et al., *Efficient and stable photocatalytic hydrogen production from water splitting over ZnxCd1–xS solid solutions under visible light irradiation.* International Journal of Hydrogen Energy, 2014. **39**(4): p. 1630-1639.

45. Yang, W., et al., *Microwave-assisted synthesis of porous CdO–CdS core–shell nanoboxes with enhanced visible-light-driven photocatalytic reduction of Cr (VI).* Journal of Materials Chemistry, 2012. **22**(28): p. 13895-13898.
46. Yuan, Y.-P., et al., *Hetero-nanostructured suspended photocatalysts for solar-to-fuel conversion.* Energy & Environmental Science, 2014. **7**(12): p. 3934-3951.
47. Zhang, J., et al., *Enhanced Visible-Light Hydrogen-Production Activity of Copper-Modified ZnxCd1− xS.* ChemSusChem, 2013. **6**(10): p. 2009-2015.
48. Gaikwad, A., et al., *Photocatalytic and photo electrochemical properties of cadmium zinc sulfide solid solution in the presence of Pt and RuS2 dual co-catalysts.* Applied Catalysis A: General, 2016. **517**: p. 91-99.
49. Hu, J.S., et al., *Mass production and high photocatalytic activity of ZnS nanoporous nanoparticles.* Angewandte Chemie International Edition, 2005. **44**(8): p. 1269-1273.
50. Gholipour, M.R., et al., *Hollow microspheres consisting of uniform ZnxCd1-xS nanoparticles with noble-metal-free co-catalysts for hydrogen evolution with high quantum efficiency under visible light.* Journal of Photochemistry and Photobiology A: Chemistry, 2018. **358**: p. 1-9.
51. Mei, Z., et al., *Hexagonal Zn 1− x Cd x S (0.2≤ x≤ 1) solid solution photocatalysts for H 2 generation from water.* Catalysis Science & Technology, 2017. **7**(4): p. 982-987.
52. Nie, Q., et al., *In situ synthesis of Zn x Cd 1− x S nanorod by a hydrothermal route.* Journal of materials science, 2004. **39**(16): p. 5611-5612.
53. Yu, J., B. Yang, and B. Cheng, *Noble-metal-free carbon nanotube-Cd 0.1 Zn 0.9 S composites for high visible-light photocatalytic H 2-production performance.* Nanoscale, 2012. **4**(8): p. 2670-2677.
54. Al Kuhaimi, S. and Z. Tulbah, *Structural, Compositional, Optical, and Electrical Properties of Solution-Grown Zn x Cd1− x S Films.* Journal of the Electrochemical Society, 2000. **147**(1): p. 214-218.
55. Yu, J., J. Zhang, and M. Jaroniec, *Preparation and enhanced visible-light photocatalytic H 2-production activity of CdS quantum dots-sensitized Zn 1− x Cd x S solid solution.* Green Chemistry, 2010. **12**(9): p. 1611-1614.
56. Sung, Y.-M., Y.-J. Lee, and K.-S. Park, *Kinetic Analysis for Formation of Cd1-x Zn x Se Solid-Solution Nanocrystals.* Journal of the American Chemical Society, 2006. **128**(28): p. 9002-9003.
57. Chen, D. and L. Gao, *Microemulsion-mediated synthesis of cadmium zinc sulfide nanocrystals with composition-modulated optical properties.* Solid state communications, 2005. **133**(3): p. 145-150.
58. Zhang, K., et al., *Significantly improved photocatalytic hydrogen production activity over Cd1-xZnxS photocatalysts prepared by a novel thermal sulfuration method.* International Journal of Hydrogen Energy, 2007. **32**(18): p. 4685-4691.
59. Wang, X., et al., *Enhanced efficiency and stability for visible light driven water splitting hydrogen production over Cd0. 5Zn0. 5S/g-C3N4 composite photocatalyst.* international journal of hydrogen energy, 2015. **40**(24): p. 7546-7552.
60. Trincado, M. and M. Vogt, *CO2-based hydrogen storage–hydrogen liberation from methanol/water mixtures and from anhydrous methanol.* Physical Sciences Reviews, 2018. **3**(9).
61. Priya, R. and S. Kanmani, *Solar photocatalytic generation of hydrogen under ultraviolet-visible light irradiation on (CdS/ZnS)/Ag 2 S+(RuO 2/TiO 2) photocatalysts.* Bulletin of Materials Science, 2010. **33**(1): p. 85-88.
62. Agopcan, B., et al., *A new sulfur source for the preparation of efficient Cd (1-x) ZnxS photocatalyst for hydrogen evolution reaction.* International Journal of Hydrogen Energy, 2018. **43**(17): p. 8206-8220.
63. Ornstein, L. *The diffraction of electromagnetic waves by a crystal*. in *KNAW, Proceedings*. 1913.
64. Bunaciu, A.A., E.G. UdriŞTioiu, and H.Y. Aboul-Enein, *X-ray diffraction: instrumentation and applications.* Critical Reviews in Analytical Chemistry, 2015. **45**(4): p. 289-299.

65. Guinier, A., *X-ray diffraction in crystals, imperfect crystals, and amorphous bodies*. 1994: Courier Corporation.
66. Egami, T. and S.J. Billinge, *Underneath the Bragg peaks: structural analysis of complex materials*. 2003: Elsevier.
67. Suryanarayana, C. and M.G. Norton, *X-ray diffraction: a practical approach*. 2013: Springer Science & Business Media.
68. Goldstein, J.I., et al., *Scanning electron microscopy and X-ray microanalysis*. 2017: Springer.
69. Amelinckx, S., et al., *Electron microscopy: principles and fundamentals*. 2008: John Wiley & Sons.
70. Ul-Hamid, A., *A Beginners' Guide to Scanning Electron Microscopy*. 2018: Springer.
71. Kuo, J., *Electron microscopy: methods and protocols*. Vol. 369. 2007: Springer Science & Business Media.
72. Hayat, M., *Principles and techniques of scanning electron microscopy. Biological applications. Volume 1.* Principles and techniques of scanning electron microscopy. Biological applications. Volume 1., 1974.
73. Zhou, W. and Z.L. Wang, *Scanning microscopy for nanotechnology: techniques and applications*. 2007: Springer science & business media.
74. Khursheed, A., *Scanning electron microscope optics and spectrometers*. 2011: World scientific.
75. Lyman, C.E., et al., *Scanning electron microscopy, X-ray microanalysis, and analytical electron microscopy: a laboratory workbook*. 2012: Springer Science & Business Media.
76. Reimer, L., *Scanning electron microscopy: physics of image formation and microanalysis*. Vol. 45. 2013: Springer.
77. Echlin, P., *Handbook of sample preparation for scanning electron microscopy and X-ray microanalysis*. 2011: Springer Science & Business Media.
78. Vernon-Parry, K., *Scanning electron microscopy: an introduction.* III-Vs Review, 2000. **13**(4): p. 40-44.
79. Reed, S.J.B., *Electron microprobe analysis and scanning electron microscopy in geology*. 2005: Cambridge university press.
80. Clark, B.J., T. Frost, and M. Russell, *UV Spectroscopy: Techniques, instrumentation and data handling*. Vol. 4. 1993: Springer Science & Business Media.
81. Fochs, P., *The measurement of the energy gap of semiconductors from their diffuse reflection spectra.* Proceedings of the Physical Society. Section B, 1956. **69**(1): p. 70.
82. Fuller, M.P. and P.R. Griffiths, *Diffuse reflectance measurements by infrared Fourier transform spectrometry.* Analytical chemistry, 1978. **50**(13): p. 1906-1910.
83. Companion, A.L., *Theory and applications of diffuse reflectance spectroscopy*, in *Developments in Applied Spectroscopy*. 1965, Springer. p. 221-234.
84. Kenkel, J., *Analytical chemistry for technicians*. 2002: CRC Press.
85. Tandon, S. and J. Gupta, *Measurement of forbidden energy gap of semiconductors by diffuse reflectance technique.* physica status solidi (b), 1970. **38**(1): p. 363-367.
86. Mirabella, F.M., *Modern techniques in applied molecular spectroscopy*. Vol. 14. 1998: John Wiley & Sons.
87. Morales, A.E., E.S. Mora, and U. Pal, *Use of diffuse reflectance spectroscopy for optical characterization of un-supported nanostructures.* Revista mexicana de física, 2007. **53**(5): p. 18-22.
88. Kortüm, G., W. Braun, and G. Herzog, *Principles and techniques of diffuse-reflectance spectroscopy.* Angewandte Chemie International Edition in English, 1963. **2**(7): p. 333-341.
89. Clark, R.N. and T.L. Roush, *Reflectance spectroscopy: Quantitative analysis techniques for remote sensing applications.* Journal of Geophysical Research: Solid Earth, 1984. **89**(B7): p. 6329-6340.
90. Gupta, A., et al., *Ultraviolet radiation in wound care: sterilization and stimulation.* Advances in wound care, 2013. **2**(8): p. 422-437.

91. Medina, B., et al., *Using new analytical approaches to verify the origin of wine*, in *New analytical approaches for verifying the origin of food*. 2013, Elsevier. p. 149-188.
92. Sur, U.K., *Surface-enhanced Raman spectroscopy.* Resonance, 2010. **15**(2): p. 154-164.
93. Hu, X., et al., *Fabrication, characterization, and application in SERS of self-assembled polyelectrolyte– gold nanorod multilayered films.* The Journal of Physical Chemistry B, 2005. **109**(41): p. 19385-19389.
94. Smith, E. and G. Dent, *Modern Raman spectroscopy: a practical approach*. 2019: Wiley.
95. Panikuttira, B. and C.P. O'Donnell, *Process Analytical Technology for the Fruit Juice Industry*, in *Fruit Juices*. 2018, Elsevier. p. 835-847.
96. Lewis, I.R. and H. Edwards, *Handbook of Raman spectroscopy: from the research laboratory to the process line*. 2001: CRC Press.
97. Hummers Jr, W.S. and R.E. Offeman, *Preparation of graphitic oxide.* Journal of the american chemical society, 1958. **80**(6): p. 1339-1339.
98. Sahu, H.R. and G.R. Rao, *Characterization of combustion synthesized zirconia powder by UV-vis, IR and other techniques.* Bulletin of Materials Science, 2000. **23**(5): p. 349-354.
99. Yan, H., et al., *Visible-light-driven hydrogen production with extremely high quantum efficiency on Pt–PdS/CdS photocatalyst.* Journal of Catalysis, 2009. **266**(2): p. 165-168.
100. Li, Q., et al., *Zn1–x Cd x S solid solutions with controlled bandgap and enhanced visible-light photocatalytic H2-production activity.* Acs Catalysis, 2013. **3**(5): p. 882-889.
101. Vinila, V., et al., *XRD studies on nano crystalline ceramic superconductor PbSrCaCuO at different treating temperatures.* Crystal Structure Theory and Applications, 2014. **3**(01): p. 1.
102. Song, Y.-W., *Carbon nanotube and graphene photonic devices: nonlinearity enhancement and novel preparation approaches*, in *Carbon Nanotubes and Graphene for Photonic Applications*. 2013, Elsevier. p. 57-97e.
103. Balandin, A.A., *Thermal properties of graphene and nanostructured carbon materials.* Nature materials, 2011. **10**(8): p. 569.
104. Murphy, A., *Band-gap determination from diffuse reflectance measurements of semiconductor films, and application to photoelectrochemical water-splitting.* Solar Energy Materials and Solar Cells, 2007. **91**(14): p. 1326-1337.
105. Reber, J.F. and K. Meier, *Photochemical production of hydrogen with zinc sulfide suspensions.* The Journal of Physical Chemistry, 1984. **88**(24): p. 5903-5913.
106. Chen, J., et al., *One-pot synthesis of CdS nanocrystals hybridized with single-layer transition-metal dichalcogenide nanosheets for efficient photocatalytic hydrogen evolution.* Angewandte Chemie International Edition, 2015. **54**(4): p. 1210-1214.
107. Jang, J.S., U.A. Joshi, and J.S. Lee, *Solvothermal synthesis of CdS nanowires for photocatalytic hydrogen and electricity production.* The Journal of Physical Chemistry C, 2007. **111**(35): p. 13280-13287.
108. Jing, D. and L. Guo, *A novel method for the preparation of a highly stable and active CdS photocatalyst with a special surface nanostructure.* The Journal of Physical Chemistry B, 2006. **110**(23): p. 11139-11145.
109. Liang, Y., et al., *Band-gap engineering of semiconductor nanowires through composition modulation.* The Journal of Physical Chemistry B, 2005. **109**(15): p. 7120-7123.
110. Genc, R., et al., *High-capacitance hybrid supercapacitor based on multi-colored fluorescent carbon-dots.* Scientific reports, 2017. **7**(1): p. 11222.
111. Aydemir, M., et al., *Photocatalytic–electrocatalytic dual hydrogen production system.* International Journal of Hydrogen Energy, 2016. **41**(19): p. 8209-8220.
112. Wang, M., et al., *Effects of sacrificial reagents on photocatalytic hydrogen evolution over different photocatalysts.* Journal of materials science, 2017. **52**(9): p. 5155-5164.
113. H. Li, X. He, Z. Kang, H. Huang, Y. Liu, J. Liu, S. Lian, C.H.A. Tsang, X. Yang, S.T. Lee *Water-soluble fluorescent carbon quantum dots and photocatalyst design,* Angewandte Chemie International Edition, 2010. **49:** p. 4430-4434

114. A. Wei, L. Xiong, L. Sun, Y. Liu, W. Li, W. Lai, X. Liu, L. Wang, W. Huang, X. Dong, *One-step electrochemical synthesis of a graphene–ZnO hybrid for improved photocatalytic activity*, Materials Research Bulletin, 2013. **48**: p. 2855-2860.
115. M. Suwarnkar, R. Dhabbe, A. Kadam, K. Garadkar, Enhanced photocatalytic activity of Ag doped TiO 2 nanoparticles synthesized by a microwave assisted method, Ceramics International, 2010. **40**: p. 5489-5496.
116. Aydemir, M., Akyüz, D., Agopcan, B., Şener, M. K., Albayrak, F. K., Sarıoğlu, C., & Koca, A. (2016). *Photocatalytic–electrocatalytic dual hydrogen production system*. International Journal of Hydrogen Energy, 2016. **41**(19): p. 8209-8220.
117. Akyüz, D. and A. Koca, *Photocatalytic hydrogen production with reduced graphene oxide (RGO)-CdZnS nano-composites synthesized by solvothermal decomposition of dimethyl sulfoxide as the sulfur source.* Journal of Photochemistry and Photobiology A: Chemistry, 2018. **364**: p. 625-634.
118. Q. Li, H. Meng, J. Yu, W. Xiao, Y. Zheng, J. Wang, *Enhanced Photocatalytic Hydrogen-Production Performance of Graphene–ZnxCd1− xS Composites by Using an Organic S Source*, Chemistry-A European Journal, 2014 **20**: p. 1176-1185.
119. P. Gao, J. Liu, S. Lee, T. Zhang, D.D. Sun, High quality graphene oxide–CdS–Pt nanocomposites for efficient photocatalytic hydrogen evolution, Journal of Materials Chemistry, 22 (2012) 2292-2298.115.
119. T. Y. Peng , K. Li , P. Zeng , Q. G. Zhang , X. G. Zhang ,*Ehanced Photoctalytic Hydroge Production Over Oxide-Cadmium Sulfide Naocomposte Under Visible Light Irradiation*, J. Phys. Chem. C ,2012 . **116**: p.22720
120. P. Zeng , Q. G. Zhang , T. Y. Peng , X. H. Zhang , *One-Pot Synthesis of Reducd Graphene Oxide-Cadmium Sulfide Nanocomposite and Its Photocatalyti c Hydrogen Production,* Phys. Chem. Chem. Phys. 2011. **13**: p.21496 .
121. M. Nguyen, P.D. Tran, S.S. Pramana, R.L. Lee, S.K. Batabyal, N. Mathews, L.H. Wong, M. Graetzel, In situ photo-assisted deposition of MoS 2 electrocatalyst onto zinc cadmium sulphide nanoparticle surfaces to construct an efficient photocatalyst for hydrogen generation, Nanoscale, 2013. **5**: p.1479-1482.
122. Y. Lu, D. Wang, P. Yang, Y. Du, C. Lu, Coupling Zn x Cd 1− x S nanoparticles with graphene-like MoS 2: superior interfacial contact, low overpotential and enhanced photocatalytic activity under visible-light irradiation, Catalysis Science & Technology, 2014. **4**: p.2650-2657.
123. P. Zeng, Q. Zhang, T. Peng, X. Zhang, *One-pot synthesis of reduced graphene oxide–cadmium sulfide nanocomposite and its photocatalytic hydrogen production*, Physical Chemistry Chemical Physics,2011. **13**: p.21496-21502.
124. Q.Li, B.Guo, J. Ran, B. Zhang,H.Yan, J.Gong, *Highly Efficient Visile-Light-Driven Photocatalytic Hydrogen Production of CdS--Cluster-Decorated Graphene Nanosheets,*Journal of The American Chemial Society, 2011 **133:** p. 10878-10884

AUTOBIOGRAPHY

Name Surname İrem Tanışık

Birth Place and Date İstanbul- 07.04.1993

Foreign Language English

E-mail iremtanisik@gmail.com

Education Background:

Degree	Department/Program	University/High School	Graduation Year
High School	Science-Maths	Kartal Anatolian High School	2011
BSc	Chemical Engineering	Yeditepe University	2016
BSc	Business Management (Open Education System)	Anadolu University	Present
MSc	Chemical Engineering	Marmara University	Present

CONGRESS/CONFERENCE

- İrem Tanışık, Duygu Akyüz, Rana Muhammad Zunain Ayaz, Özlem Uğuz, Cevat Sarıoğlu, Fatma Karaca Albayrak, Ali Rıza Özkaya, Atıf Koca
  Active Photocatalysts Designed by Sulphurization Method for Hydrogen Production, 3rd International Hydrogen Technologies Congress, Alanya, Turkey